JOURNAL OF PETROLOGY | VOLUME 50 | NUMBER 7 | PAGES 1267–1298 | 2009 | doi:10.1093/petrology/egp021

Heterogeneous Lithospheric Mantle beneath Northern Patagonia: Evidence from Prahuaniyeu Garnet- and Spinel-Peridotites

ERNESTO A. BJERG[1], THEODOROS NTAFLOS[2]*, MARTIN THÖNI[2], PAOLA ALIANI[1] AND CARLOS H. LABUDIA[1]

[1]INSTITUTO GEOLOGICO DEL SUR, CONICET AND DEPARTMENTO DE GEOLOGIA, UNIVERSIDAD NACIONAL DEL SUR, SAN JUAN 670, 8000 BAHIA BLANCA, ARGENTINA

[2]DEPARTMENT OF LITHOSPHERIC RESEARCH, UNIVERSITY OF VIENNA, ALTHANSTR. 14, VIENNA, AUSTRIA

RECEIVED JUNE 4, 2008; ACCEPTED MARCH 26, 2009
ADVANCE ACCESS PUBLICATION MAY 11, 2009

Prahuaniyeu, located on the NW margin of the Somoncura Large Igneous Province in northern Patagonia, is one of two known localities in Argentina where mantle-derived garnet- and spinel-bearing peridotites occur associated with alkali basalts; the other locality is the Pali Aike volcanic field of southern Patagonia. Most of the Prahuaniyeu garnet-bearing peridotites are fertile in terms of their Al_2O_3 and CaO contents, whereas the spinel-bearing peridotites cover a wide range from fertile to depleted compositions. Whole-rock light rare earth element (LREE) enrichment in the garnet-bearing peridotites and partly in the spinel-peridotites is consistent with intergranular percolation of the host basalt melt, as hydrous phases are not present and the clinopyroxenes and garnets are not enriched in LREE. Lack of slab-derived component(s) in the metasomatic products rules out the participation of a subducted slab in the generation of these basalts. In situ *clinopyroxene analyses suggest that a group of spinel-peridotites experienced cryptic metasomatism by carbonatitic melts. Non-metasomatized garnet- and spinel-peridotites have experienced fractional melting ranging from 1 to 3% and from 5 to 12%, respectively. The Prahuaniyeu xenoliths lie on an elevated geotherm (high temperatures at low pressure) implying convective heat transport. The two most fertile samples, which indicate apparent internal 'ages' between c. 10 and 30 Ma for the sub-Prahuaniyeu lithospheric mantle, suggest resetting of the Sm–Nd isotopic system under a high-temperature regime and most probably reflect closure of the system following this 'high-T event', which can be related to extensive magmatic activity within the Somoncura province, starting in the Eocene and finishing in the Miocene.*

KEY WORDS: *mantle xenoliths; garnet-peridotite; spinel-peridotite; northern Patagonia; metasomatism; Prahuaniyeu*

INTRODUCTION

Mantle xenoliths brought to the surface by basaltic lavas provide invaluable information for the study of mantle processes and the nature of the lithospheric mantle. In both oceanic and continental environments, spinel-peridotites are the commonest xenoliths in alkali basalts. Garnet-bearing xenoliths from alkali basalts are less common, but have been recorded from the Baikal region (Ionov *et al.*, 1993; Glaser *et al.*, 1999; Litasov & Taniguchi, 2002), in southern Patagonia (Skewes & Stern, 1979; Stern *et al.*, 1989, 1999; Kempton *et al.*, 1999*a*, 1999*b*; Wang *et al.*, 2008), southeastern China (Xu *et al.*, 2000), Lashaine, Tanzania (Dawson *et al.*, 1970; Henjes-Kunst & Altherr, 1992) and SE Australia (Sutherland & Hollis, 1982). Whereas garnet-peridotite xenoliths are sparse in alkali basalts, they are abundant in kimberlites and related rocks. In general, kimberlites mainly carry garnet-peridotite xenoliths from the deeper lithospheric mantle whereas alkali basalts are the host lavas for garnet-peridotite xenoliths derived from depths of <140 km. Kimberlites occur exclusively in Archean cratons and alkali basalts mostly in younger lithospheric domains.

*Corresponding author. Telephone: (+43) 1 4277 53314. Fax: (+43) 1 4277 9533. E-mail: theodoros.ntaflos@univie.ac.at

In alkali basalts, spinel–garnet-peridotite xenoliths are commoner than garnet-peridotites. They are of particular interest because they define the transition zone from garnet-peridotite to spinel-peridotite facies. The estimation of the P–T conditions in such mantle xenoliths provides, more or less, the maximum depth at which spinel-peridotites are stable.

Cenozoic lavas are widely distributed in Patagonia. According to Stern *et al.* (1989), they are related to subduction of oceanic lithosphere beneath the western continental margin of the South American plate. Gorring *et al.* (1997) and Gorring & Kay (2001) postulated that magmatism in Patagonia SE of the Chile Triple Junction was related to the opening of an asthenospheric 'slab window' produced by ridge–trench collision.

The mantle xenoliths in the Pliocene alkali basalts of the Pali Aike volcanic field in southernmost Patagonia are garnet-peridotites, spinel–garnet-peridotites and spinel-peridotites (Stern *et al.*, 1989; Kempton *et al.*, 1999*a*, 1999*b*). The P–T history (Kempton *et al.*, 1999a) indicates that spinel–garnet-peridotites occur at depths between 50 and 80 km and that there is a temperature overlap between garnet-bearing and garnet-free xenoliths, indicating a scattering of both lithologies over a significant depth interval beneath Pali Aike. Lead isotope data suggest that the Pali Aike xenoliths have been affected by metasomatic fluids that were not derived from subduction of modern-day sediments but from interaction with migrating silicate melts generated in equilibrium with garnet (Kempton *et al.*, 1999*b*).

The Prahuaniyeu mantle xenolith suite from northern Patagonia is the only other known occurrence of garnet-bearing peridotites in South America. Like Pali Aike, the Prahuaniyeu xenolith suite contains garnet-peridotites, spinel–garnet-peridotites and spinel-peridotites.

In this study we present the first detailed mineral chemistry data (major and trace elements), obtained by both electron microprobe and laser ablation inductively coupled plasma mass spectrometry (LA-ICP-MS), as well as Nd–Sm isotopic data for garnet-bearing and garnet-free peridotites from Prahuaniyeu. Based on these data, we discuss the evolution of the lithospheric mantle beneath northern Patagonia and compare our results with other garnet-bearing xenoliths from other localities worldwide and especially from Pali Aike.

GEOLOGICAL SETTING

Southern South America between latitudes 40° and 52°S (Fig. 1) is divided into two regions: (1) the Patagonian Cordillera, located at the western active margin of the South American plate, related to the subduction of the Nazca and Antarctic plates; (2) the extra-Andean domain, which represents a passive continental margin located in the eastern part of the region (Fig. 1). The extra-Andean domain is further subdivided into northern and southern units along latitude 46°30′S. The dividing zone lies on the extension of the Chile Triple Junction, which is characterized by an absence of volcanic arc activity (Fig. 1).

Late Oligocene to Neogene plateau basalts are widespread in the extra-Andean region, covering an area of *c.* 120 000 km^2. Pleistocene to recent xenolith-bearing alkali basalts are not particularly abundant but occur within the extra-Andean region. The late Oligocene to early Miocene plateau basalts of Somoncura, which form the largest magmatic province north of 46°30'S, consist of basalts, trachybasalts, basaltic andesites and trachyandesites. On a regional scale, the basement north of 46°30′S consists of low-grade metamorphic rocks (pre-Permian), granites, granodiorites, ignimbrites and granophyres (Late Permian–Early Triassic), conglomerates, sandstones and pyroclastic acidic rocks (Middle to Late Triassic), rhyolites (Late Triassic to Early Jurassic), andesitic rocks (Late Jurassic), coastal and marine sediments (Maastrichtian–Danian), continental sediments, the Somoncura Plateau basaltic lavas and tuffs (Pliocene), and xenolith-bearing alkaline basalts (Pliocene–Pleistocene) (Nullo, 1978; Stipanicic & Methol, 1980; Llambías & Rapela, 1984; Labudía & Bjerg, 1994; Saini-Eidukat *et al.*, 1999; Bjerg *et al.*, 2005).

ANALYTICAL PROCEDURES

Collected xenoliths range from 5 to 15 cm in diameter. To ensure representative analyses only xenoliths between 10 and 15 cm in diameter were used for whole-rock chemistry.

Major and trace element analyses were carried out by X-ray fluorescence (XRF) spectrometry (Philips 2400). Quantitative XRF determinations for major element oxides were made on fused glass discs using a mixture of 1·2 g sample and 6 g flux ($Li_2B_4O_7$). The mixtures were fused using a Philips Perl'X3 automatic bead machine under controlled conditions in a Pt–Au crucible, and poured into a (Pt–Au)–gold dish. The Philips SuperQ software was used for matrix corrections. Trace element determinations were carried out on pressed powder pellets using the offline in-house program 'Traces' written by K. Petrakakis at the Institute of Petrology, Vienna, for background, mass absorption and interference corrections. Comparison of these data with a set of the geochemical reference standards (GSR-1 to GSR-6) suggests uncertainties in the range 5–10% for all major and trace elements. Scandium contents for all samples and the REE content of the host basalts were determined by instrumental neutron activation analysis (INAA) using the method described by Kruse & Spettel (1979). The analytical error was in the range of 10%. Rare earth elements were analyzed by ICP-MS (ELAN 6100) at the University of Vienna, Department of Lithospheric Sciences.

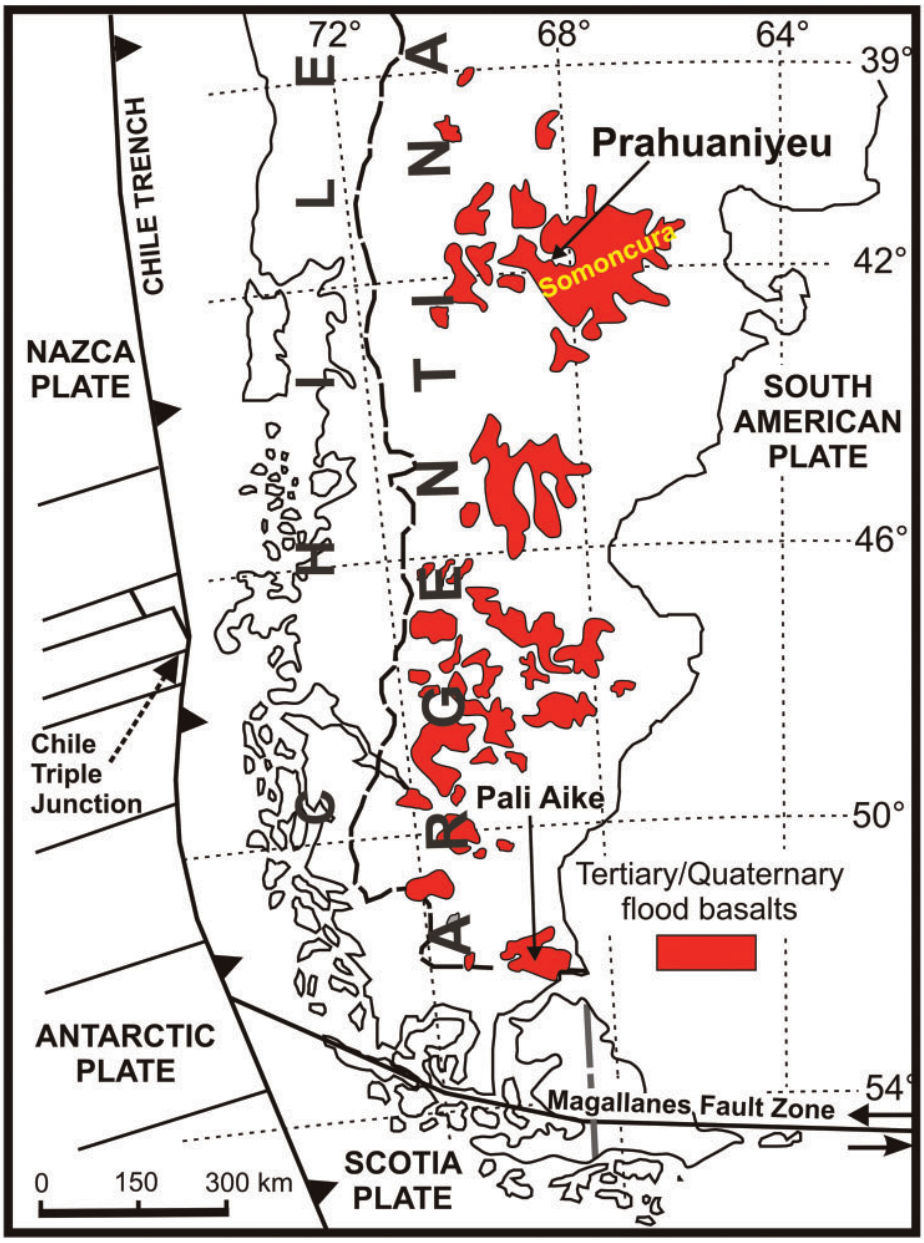

Fig. 1. Simplified geological map of Patagonia, modified from Gorring *et al.* (1997). The arrows indicate the garnet-bearing mantle xenolith locations Prahuaniyeu and Pali Aike.

Major element analyses of minerals and glasses were carried out using a Cameca SX100 electron microprobe at the University of Vienna. The operating conditions for minerals were 15 kV and 20 nA. To reduce alkali migration in glasses, analyses were performed using a defocused beam with a diameter of 5–10 μm at 15 kV and 10 nA. The error for all elements was below 5%, except for Na, the error of which was in the range of 10%. Natural and synthetic standards were used for calibration and a PAP correction was applied to the data. Modal mineral compositions were calculated from microprobe analyses of single minerals and bulk-rock compositions in combination with point-counting polished thin-sections of areas ranging from 6 to 8 cm^2 and an average grain size between 2 and 2·4 mm.

Trace element abundances in clinopyroxenes and garnets were determined *in situ* by LA-ICP-MS at the Department

of Earth Sciences, Memorial University of Newfoundland, St. John's, Newfoundland. The laser beam of a Q-switched Nd:YAG laser operated at 266 nm in the UV region was coupled to a Fisons VG PQ2.ICP-MS instrument. The laser beam energy was $0{\cdot}4 \pm 0{\cdot}6$ mJ per pulse and the diameter of the ablation pits was about 40–50 μm. The silicate glass NIST 612 was used for calibration and BCR-2 glass was used as secondary standard. Calcium was used as an internal standard to correct the ablation yield calculations. Data reduction was performed using the LAMTRACE® spreadsheet software written in-house by S. Jackson. Typical theoretical detection limits are in the range of 10–20 ppb for REE, Ba, Th, U, Nb, Ta, Sr, Zr, and Hf.

RESULTS

Petrographic description

The modal composition of the garnet-peridotites (Table 1) shows that they are lherzolites with high modal proportions of clinopyroxene. A striking difference between the two garnet lherzolites Pra199 and Pra302 is the low olivine and high orthopyroxene modal proportions in the latter. Garnets in Pra302 are fine-grained (up to 1 mm diameter) with a relatively wide corona of kelyphitic alteration. Some garnets have been entirely kelyphitized. In contrast, garnets in sample Pra199 are coarse grained (up to 4 mm in diameter) and have a narrow corona of kelyphytic alteration and inclusions of olivine and coexisting clinopyroxene–orthopyroxene (Fig. 2a and b). The matrix clinopyroxenes, compared with olivine and orthopyroxene, are relatively fine grained (up to 1 mm diameter) with irregular curvilinear grains. Spinel–garnet-peridotites are characterized by a foliated texture, defined by olivine (Fig. 2c and d). Garnet grains, compared with those from the garnet-peridotites, are generally smaller (rarely up to 1 mm diameter) and lack inclusions. Orthopyroxene grains partly have the same orientation as olivines whereas clinopyroxene grains are small (up to 1 mm diameter). Brown, rounded to elongated spinels formed in the triple junctions between olivine, clinopyroxene and othopyroxene are usually not associated with garnets (Fig. 2c and d).

The majority of the studied spinel-peridotites, like the garnet-peridotites, have a foliated texture with tabular olivines. Spinels are either intergranular or form worm-like pockets associated with orthopyroxenes (Fig. 2e and f). Spinel-peridotites with medium-grained protogranular texture are also present (Fig. 2g); olivine grains are euhedral to sub-euhedral and curvilinear othopyroxene grains are frequently associated with fine-grained clinopyroxene. Fine-grained spinels form interstitial grains in triple junction points. Typical worm-like thin spinel lamellae and blebs closely associated with orthopyroxene indicate that they have been exsolved from the orthopyroxene (Fig. 2h). Exsolution lamellae were not observed in either orthopyroxene or clinopyroxene in any of the studied peridotites.

Bulk-rock chemistry

Major and trace element analyses are given in Table 2. Both garnet- and spinel-bearing xenoliths have a wide range of CaO and Al_2O_3 contents (0·51–4·54 and 0·90–4·31 wt%, respectively), representing a suite of xenoliths that covers the whole spectrum from fertile to depleted compositions. The CaO content (4·54 wt%) of garnet-peridotite Pra302 is higher than that of inferred primitive mantle (CaO 3·54 wt%, McDonough & Sun, 1995). Both CaO and Al_2O_3 correlate well with MgO and define linear trends (Fig. 3a and b). The slight deviation from linearity of the most depleted samples is consistent with the general trend predicted by O'Neil & Palme (1998). Excepting that, among the collected samples, the most depleted xenoliths are spinel-peridotites, there are no significant compositional differences between garnet- and spinel-bearing xenoliths. Other major elements, such as SiO_2, TiO_2, and Na_2O, show similar negative correlations with MgO. In contrast, Sr and the light rare earth elements (LREE) define two trends when plotted against MgO; in trend (A) Sr and La correlate antithetically

Table 1: Calculated modal composition of mantle xenoliths from Prahuaniyeu, northern Patagonia, Argentina

	Spinel-peridotites													Spinel–garnet-peridotites					Garnet-peridotites	
Sample:	Pra79	Pra82	Pra91	Pra94	Pra96	Pra98	Pra232	Pra233	Pra301	Pra303	Pra305	Pra306	Pra307	Pra70	Pra74	Pra197	Pra198	Pra234	Pra199	Pra302
ol	55·7	60·1	57·8	89·4	75·4	69·5	51·5	57·9	69·8	70·8	71·0	72·1	61·9	80·1	64·6	*73·0*	68·4	55·9	56·8	40·9
opx	30·0	32·0	23·2	6·4	21·0	25·1	29·1	24·7	26·1	24·6	26·8	24·3	29·7	15·2	23·3	*20·2*	16·6	22·1	19·7	33·9
cpx	11·9	7·2	17·0	3·0	2·6	5·2	16·0	15·4	3·4	3·8	1·3	3·1	6·6	3·0	10·8	*5·1*	9·3	11·5	17·4	18·7
sp	2·1	0·7	1·9	1·2	0·8	0·3	2·5	2·0	0·6	0·5	0·8	0·5	1·1	0·1	tr	*0·1*	0·1	tr		
gt														1·6	1·1	*1·5*	5·4	9·6	5·1	6·2
Total	99·7	99·9	99·9	100·0	99·8	100·1	99·1	100·0	99·9	99·6	99·9	100·0	99·3	99·9	99·8	*99·9*	99·8	99·1	99·0	99·7

tr, trace; italic numbers, modal composition based on 7000 point counts.

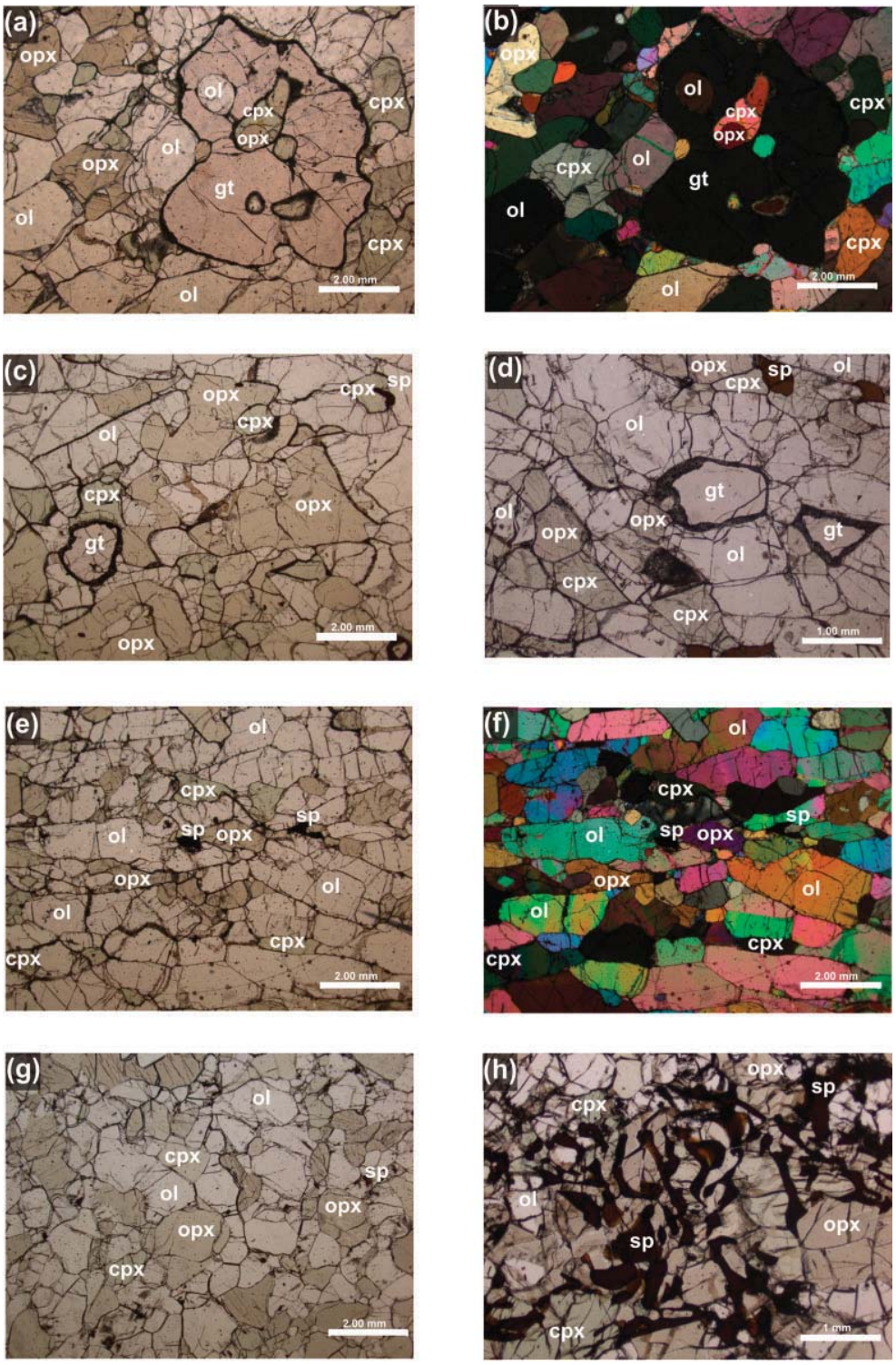

Fig. 2. Photomicrographs of Prahuaniyeu mantle xenoliths. (a) Garnet lherzolite in plane-polarized light (PPL). Poikilitically enclosed by the coarse-grained garnet are small olivine, clinopyroxene and coexisting orthopyroxene–clinopyroxene grains. (b) Same as (a) under cross-polarized light (XPL). (c) Garnet–spinel-lherzolite with a foliated texture. Spinel is not associated with garnet and grows interstitially (PPL). (d) Closer view of a spinel–garnet-harzburgite with a foliated texture. Garnet shows a thin kelyphitic rim. The brown spinel is not associated with garnet. (e) Foliated spinel lherzolite (PPL). (f) As in (e) but under XPL. (g) Spinel lherzolite with protogranular texture (PPL). (h) Worm-like spinel blebs and lamellae closely associated with orthopyroxene from which they have apparently been exsolved (PPL).

Table 2: Major and trace element analyses of Prahuaniyeu mantle xenoliths, northern Patagonia, Argentina

	Spinel-peridotites																
Sample:	Pra4	Pra5	Pra46	Pra57	Pra68	Pra79	Pra82	Pra91	Pra94	Pra95	Pra96	Pra98	Pra231	Pra232	Pra233	Pra301	Pra303
wt%																	
SiO_2	44·1	45·6	45·5	44·5	44·5	45·6	46·2	44·9	44·1	44·9	44·0	45·1	42·2	44·5	45·2	44·9	44·7
TiO_2	0·053	0·091	0·044	0·037	0·048	0·084	0·033	0·272	0·037	0·144	0·078	0·099	0·049	0·075	0·160	0·024	0·033
Al_2O_3	1·12	2·80	2·18	1·24	1·81	3·36	1·70	3·88	1·01	1·46	1·20	1·87	0·90	2·17	3·73	1·23	1·24
$Fe_2O_3^*$	8·29	8·22	8·66	8·37	9·00	8·52	8·01	9·25	8·88	8·37	8·48	8·92	9·01	8·83	9·10	8·52	8·58
MnO	0·12	0·12	0·12	0·12	0·13	0·13	0·12	0·13	0·13	0·12	0·12	0·13	0·12	0·13	0·13	0·12	0·12
MgO	45·2	41·5	41·9	44·6	43·4	39·9	42·6	38·5	45·9	43·6	45·5	43·5	46·7	42·8	38·9	45·2	44·9
CaO	0·91	2·48	2·37	0·86	1·64	2·71	1·84	3·45	0·79	1·25	0·87	1·37	0·79	2·28	3·17	1·05	1·20
Na_2O	0·119	0·152	0·140	0·041	0·083	0·189	0·070	0·272	0·045	0·086	0·126	0·073	0·075	0·126	0·285	0·023	0·063
K_2O	0·050	0·012	0·016	0·014	0·017	0·019	0·013	0·024	0·012	0·067	0·059	0·017	0·048	0·012	0·008	0·005	0·027
P_2O_5	0·085	0·017	0·060	0·036	0·052	0·032	0·085	0·144	0·026	0·090	0·105	0·049	0·043	0·045	0·021	0·081	0·048
Total	100·00	100·96	101·05	99·86	100·72	100·58	100·71	100·83	101·01	100·10	100·55	101·19	99·91	100·96	100·69	101·18	100·88
ppm																	
Nb	3	1	1	1	1	2	1	2	1	3	2	1	1	1	1	1	2
Zr	7	5	4	4	4	6	6	11	4	9	7	6	5	4	8	3	5
Y	1·80	1·36	1·07	1·70	1·30	1·36	0·70	2·48	0·36	1·90	0·45	0·86	1·50	1·34	1·80	0·27	0·34
Sr	42	12	13	12	11	14	21	29	9	27	29	16	16	12	23	20	21
Rb	1·3	0·9	0·9	1·0	1·0	1·0	0·9	0·9	1·0	1·3	1·4	0·9	1·3	0·9	0·7	0·6	1·1
Ga	1	5	4	1	4	5	3	7	4	1	4	4	2	5	6	3	4
Zn	39	62	63	38	66	64	57	71	62	37	63	63	40	64	69	59	61
Cu	12	18	17	11	4	3	2	16	4	12	8	6	14	8	11	2	4
Ni	2301	2045	2240	2061	2153	1931	2083	1910	2353	1934	2430	2169	2306	2152	1923	2340	2372
Co	102	94	99	98	105	94	96	93	111	91	110	105	108	101	95	106	107
Cr	2695	3401	2865	3422	2491	3224	3486	2541	2448	2714	3285	2561	2131	2878	2719	2820	2682
Sc	6·2	9·4	8·5	5·9	7·4	11·8	7·6	11·4	6·0	6·5	6·0	8·6	5·5	10·2	10·1	6·2	6·3
V	24	51	41	28	23	47	47	75	26	35	39	45	31	67	74	42	36
La	*2·283*	*0·786*	*0·834*	*0·965*	*1·162*	*0·930*	*0·963*	*1·430*	*0·414*	*2·531*	*1·022*	*0·572*	*1·283*	*0·652*	*1·196*	*0·237*	*1·024*
Ce	*5·875*	*1·462*	*1·591*	*1·563*	*2·647*	*1·352*	*1·722*	*3·098*	*0·852*	*5·285*	*1·864*	*1·276*	*2·235*	*1·244*	*2·018*	*0·460*	*1·229*
Pr	*0·626*	*0·141*	*0·192*	*0·192*	*0·273*	*0·162*	*0·212*	*0·348*	*0·101*	*0·586*	*0·232*	*0·151*	*0·273*	*0·162*	*0·202*	*0·061*	*0·121*
Nd	*2·250*	*0·553*	*0·693*	*0·653*	*1·025*	*0·653*	*0·884*	*1·397*	*0·402*	*1·896*	*0·894*	*0·603*	*0·985*	*0·683*	*0·904*	*0·241*	*0·462*
Sm	*0·382*	*0·191*	*0·181*	*0·134*	*0·231*	*0·190*	*0·241*	*0·362*	*0·100*	*0·401*	*0·251*	*0·171*	*0·271*	*0·171*	*0·261*	*0·060*	*0·131*
Eu	*0·111*	*0·070*	*0·050*	*0·040*	*0·070*	*0·064*	*0·067*	*0·135*	*0·030*	*0·121*	*0·070*	*0·056*	*0·080*	*0·060*	*0·090*	*0·016*	*0·040*
Gd	*0·281*	*0·221*	*0·141*	*0·100*	*0·211*	*0·211*	*0·181*	*0·452*	*0·083*	*0·336*	*0·170*	*0·152*	*0·201*	*0·211*	*0·342*	*0·041*	*0·100*
Tb	*0·040*	*0·040*	*0·020*	*0·010*	*0·030*	*0·040*	*0·021*	*0·073*	*0·011*	*0·047*	*0·020*	*0·020*	*0·031*	*0·034*	*0·060*	*0·006*	*0·013*
Dy	*0·171*	*0·271*	*0·161*	*0·060*	*0·191*	*0·281*	*0·113*	*0·492*	*0·060*	*0·241*	*0·110*	*0·131*	*0·138*	*0·241*	*0·381*	*0·039*	*0·070*
Ho	*0·030*	*0·060*	*0·040*	*0·011*	*0·040*	*0·063*	*0·020*	*0·100*	*0·011*	*0·050*	*0·020*	*0·030*	*0·022*	*0·050*	*0·080*	*0·009*	*0·013*
Er	*0·080*	*0·181*	*0·120*	*0·040*	*0·121*	*0·214*	*0·063*	*0·311*	*0·048*	*0·175*	*0·050*	*0·100*	*0·070*	*0·171*	*0·251*	*0·030*	*0·042*
Tm	*0·010*	*0·030*	*0·020*	*0·006*	*0·020*	*0·040*	*0·010*	*0·048*	*0·009*	*0·037*	*0·007*	*0·017*	*0·010*	*0·027*	*0·037*	*0·006*	*0·009*
Yb	*0·070*	*0·191*	*0·140*	*0·040*	*0·172*	*0·321*	*0·069*	*0·291*	*0·067*	*0·291*	*0·050*	*0·110*	*0·060*	*0·181*	*0·231*	*0·048*	*0·050*
Lu	*0·010*	*0·030*	*0·020*	*0·010*	*0·032*	*0·063*	*0·011*	*0·043*	*0·011*	*0·050*	*0·010*	*0·019*	*0·010*	*0·030*	*0·034*	*0·010*	*0·010*
Th	*0·13*	*0·67*	*0·22*	*0·19*	*0·30*	*0·39*	*0·16*	*0·13*	*0·11*	*0·11*	*0·79*	*0·11*	*0·17*	*0·18*	*0·06*	*0·06*	*0·15*

(continued)

Table 2: Continued

	Spinel-peridotites				Spinel–garnet-peridotites				Garnet-peridotite		Host basalt
Sample:	Pra304	Pra305	Pra306	Pra307	Pra70	Pra74	Pra198	Pra234	Pra199	Pra302	
wt%											
SiO_2	45·0	44·9	45·2	45·1	43·82	44·84	43·24	44·98	45·49	47·97	39·74
TiO_2	0·080	0·061	0·078	0·052	0·06	0·104	0·0891	0·0786	0·1782	0·0939	3·25
Al_2O_3	2·89	1·12	1·08	1·83	1·31	2·4	2·76	2·03	3·83	4·31	9·65
Fe_2O_3*	8·93	9·73	8·20	8·50	9·35	8·89	9·01	9·53	9·42	8·43	14·49
MnO	0·13	0·12	0·12	0·12	0·12	0·12	0·13	0·13	0·13	0·14	0·22
MgO	40·3	44·6	45·4	43·0	45·47	41·78	42·12	42·23	38·24	35·7	13·63
CaO	2·50	0·51	0·90	1·87	0·96	2·35	2·42	1·8	3·57	4·54	11·39
Na_2O	0·158	0·058	0·117	0·043	0·0597	0·1859	0·1398	0·1119	0·2987	0·1881	4·29
K_2O	0·056	0·028	0·019	0·022	0·0165	0·0133	0·0434	0·0185	0·0113	0·0347	1·20
P_2O_5	0·170	0·080	0·168	0·093	0·0397	0·0174	0·042	0·0155	0·0218	0·0458	1·40
Total	100·22	101·23	101·23	100·66	101·23	100·77	99·99	100·96	101·29	101·45	99·26
ppm											
Nb	4	2	2	1	1·2	1·0	3·6	1·2	1·0	1·9	123
Zr	7	13	6	5	4·9	5·4	3·7	4·8	8·9	5·1	509
Y	0·95	0·89	1·70	0·51	0·64	1·12	1·70	0·58	2·67	1·66	42·8
Sr	32	30	41	19	9·718	13·06	12	10·17	17·22	15·99	1503
Rb	1·3	1·0	0·9	1·1	0·894	1·024	1·16	0·963	1·136	1·058	17·1
Ga	3	5	4	4	4·2	5·1	2·2	4·9	6·5	5·8	23
Zn	47	94	61	60	68	67	43	75	72	58	130
Cu	19	5	7	11	8·8	11	16·9	10	14	2·5	47·2
Ni	2036	2542	2198	2349	2469	2155	2093	2233	1877	1708	376
Co	99	114	100	105	114	100	99	106	96	81	55
Cr	3072	2274	2780	3058	1862·3	2952·4	2406·0	2881·9	2643·8	2422·6	467
Sc	7·6	3·6	7·1	5·8	5·0	8·3	10·3	9·0	12·0	13·6	16·8
V	47	14	46	40	30	57	49	57	80	102	170
La	*1·742*	*1·475*	*1·474*	*0·767*	*0·718*	*0·423*	*0·961*	*0·356*	*0·449*	*0·564*	106
Ce	*3·573*	*3·229*	*2·965*	*1·000*	*1·247*	*0·951*	*1·620*	*0·661*	*1·082*	*0·981*	219
Pr	*0·353*	*0·404*	*0·313*	*0·148*	*0·172*	*0·141*	*0·212*	*0·081*	*0·189*	*0·131*	
Nd	*1·256*	*1·658*	*1·361*	*0·522*	*0·604*	*0·673*	*0·814*	*0·352*	*1·026*	*0·553*	83
Sm	*0·261*	*0·384*	*0·311*	*0·131*	*0·125*	*0·205*	*0·231*	*0·111*	*0·362*	*0·181*	16
Eu	*0·090*	*0·121*	*0·100*	*0·040*	*0·045*	*0·067*	*0·090*	*0·038*	*0·131*	*0·070*	4·9
Gd	*0·309*	*0·342*	*0·321*	*0·121*	*0·162*	*0·229*	*0·332*	*0·111*	*0·468*	*0·251*	
Tb	*0·049*	*0·040*	*0·055*	*0·020*	*0·027*	*0·039*	*0·060*	*0·020*	*0·092*	*0·048*	1·772
Dy	*0·331*	*0·211*	*0·305*	*0·110*	*0·141*	*0·237*	*0·391*	*0·132*	*0·599*	*0·341*	
Ho	*0·080*	*0·040*	*0·078*	*0·020*	*0·030*	*0·052*	*0·100*	*0·030*	*0·130*	*0·080*	
Er	*0·231*	*0·110*	*0·231*	*0·063*	*0·083*	*0·140*	*0·271*	*0·090*	*0·401*	*0·251*	
Tm	*0·040*	*0·017*	*0·039*	*0·010*	*0·014*	*0·022*	*0·040*	*0·014*	*0·064*	*0·040*	
Yb	*0·291*	*0·110*	*0·264*	*0·070*	*0·089*	*0·130*	*0·291*	*0·089*	*0·413*	*0·261*	2·561
Lu	*0·047*	*0·020*	*0·040*	*0·011*	*0·020*	*0·020*	*0·040*	*0·013*	*0·064*	*0·040*	0·278
Th	*0·29*	*0·27*	*0·02*	*0·08*	*<0·01*	*<0·01*	*0·01*	*0·03*	*<0·01*	*0·03*	16·1

Italic numbers ICP-MS, underlined numbers INAA.*Total Fe as Fe_2O_3.

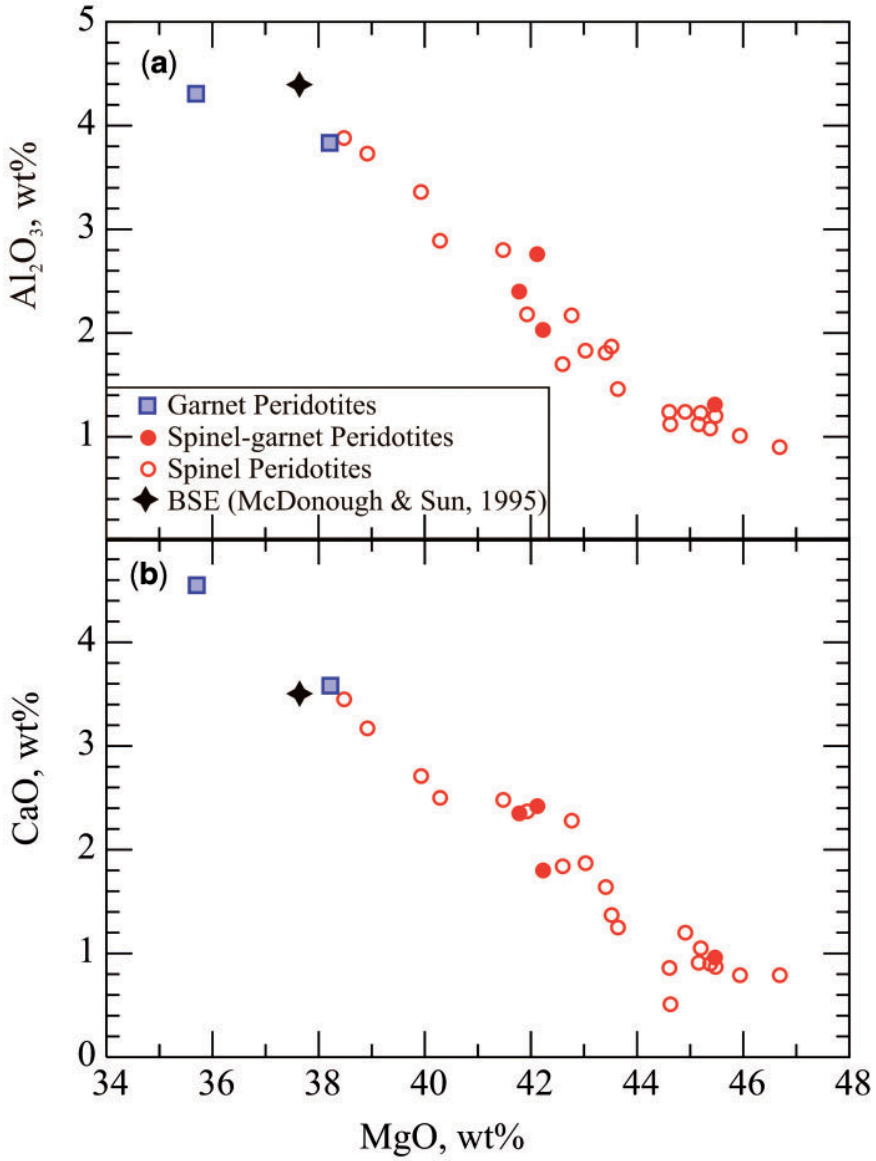

Fig. 3. Major element variations in whole-rock Prahuaniyeu peridotites. (a) MgO vs Al_2O_3; (b) CaO vs MgO.

with MgO, suggesting melt depletion processes, whereas in trend (B) they increase at almost constant MgO, suggesting enrichment through metasomatic processes (Fig. 4a and b).

Whole-rock Primitive Mantle (PM; McDonough & Sun, 1995) normalized REE patterns of garnet-bearing peridotites (Fig. 5a) are relatively flat in the heavy REE (HREE) and middle REE (MREE), whereas the LREE are enriched compared with the HREE. The HREE range between slightly depleted (~1 × PM) to strongly depleted (0·2 × PM), indicating variable degrees of partial melting. Sample Pral99, a fertile garnet-peridotite, has a REE pattern very close to that of the Primitive Mantle.

The whole-rock REE patterns from spinel-peridotites have been divided into two groups. Group 1 shows essentially flat PM-normalized patterns (Fig. 5b) with HREE ranging from 0·3 × PM to 0·9 × PM. The xenoliths have relatively flat HREE patterns and slightly enriched LREE, giving $(La/Yb)_N = 3–5$. Group 2 includes samples with HREE (0·16–0·8) × PM that have been strongly enriched in LREE (Fig. 5c), giving high $(La/Yb)_N$, of 8–16.

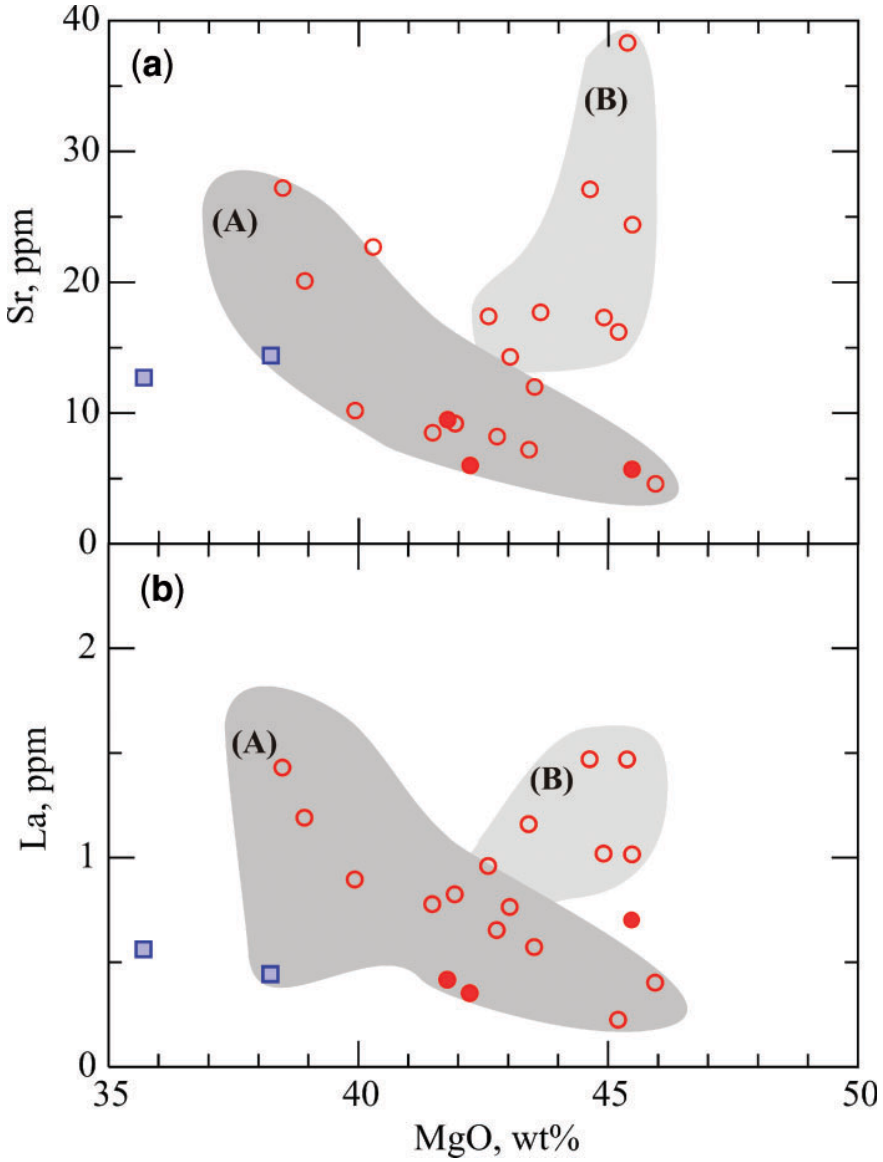

Fig. 4. Sr and La (ppm) vs MgO (wt%) define two trends: in trend (A) Sr and La correlate negatively with MgO, suggesting melt depletion processes, whereas in trend (B) both Sr and La increase with increasing MgO, indicating enrichment through metasomatic processes.

Mineral chemistry

Olivine

Olivine microprobe analyses are given in Table 3. The two garnet-bearing peridotites Pra199 and Pra302 have compositions of $Fo_{89.6}$ and $Fo_{89.3}$, respectively. The spinel–garnet-bearing peridotites have olivine compositions ranging from $Fo_{89.5}$ to $Fo_{91.2}$ whereas the spinel-peridotites have, in general, a slightly higher Fo range, between $Fo_{89.5}$ and $Fo_{91.7}$. Olivines in the garnet-bearing peridotites have higher CaO concentrations (CaO ranges from 0·09 to 0·14 wt%) than in the spinel-bearing peridotites (0·03 and 0·13 wt%). An exception is olivine in a rather depleted spinel-lherzolite, Pra307, which has an unusually high CaO content (0·17 wt%). Without excluding the possibility that this sample is modally enriched in clinopyroxene, the elevated CaO content seems to be consistent with the relatively high whole-rock CaO/Al_2O_3 ratio of 1·02.

Orthopyroxene

Orthopyroxene microprobe analyses are given in Table 4. They are all enstatite in composition with a very narrow range of mg-number (0·90–0·92), slightly higher than

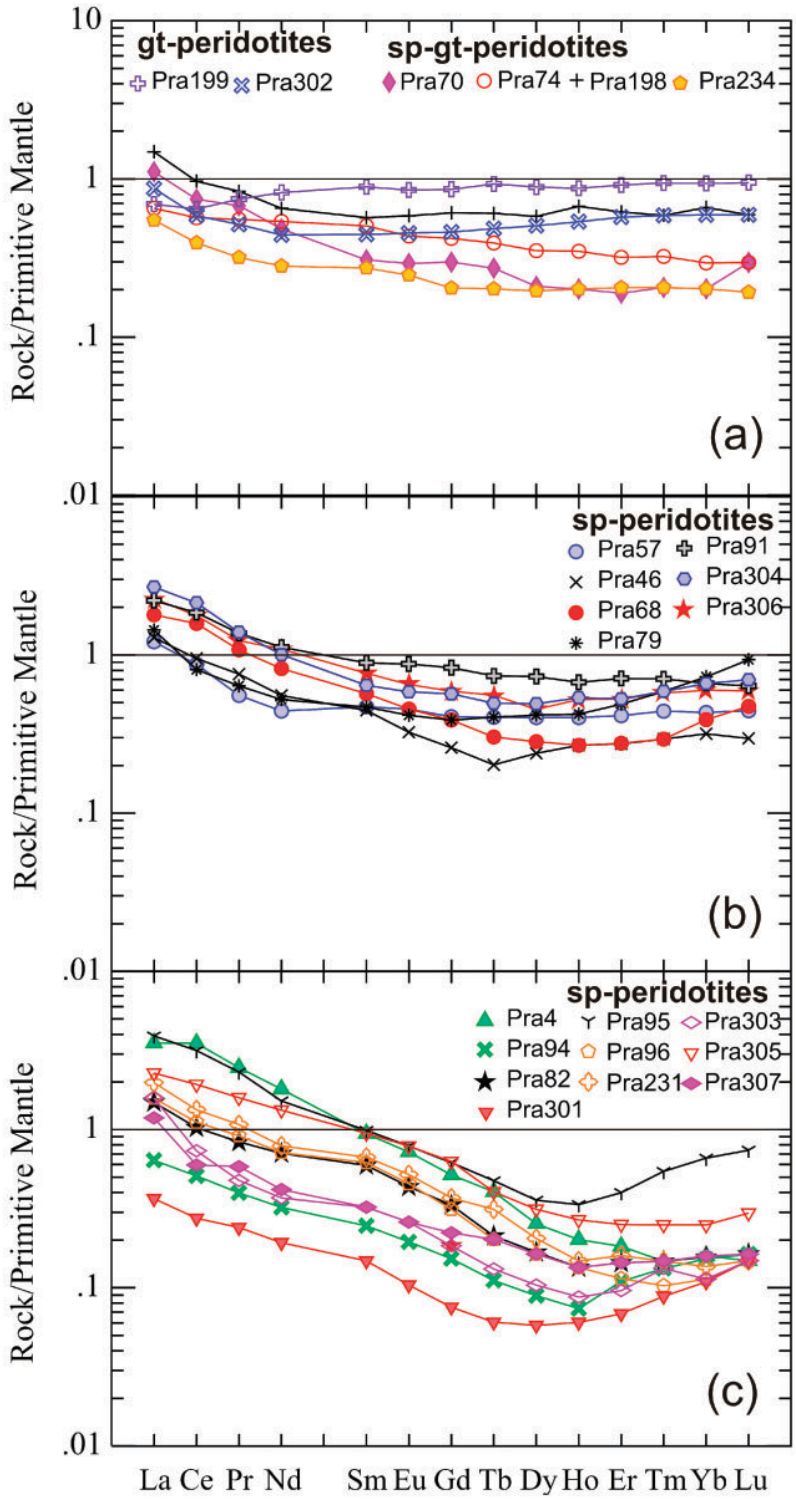

Fig. 5. Whole-rock REE patterns for Prahauniyeu garnet- and spinel–garnet-peridotites (a), (b) and (c) spinel-peridotites.

Table 3: Electron microprobe analyses of olivine from Prahuaniyeu peridotite xenoliths, northern Patagonia, Argentina

	Spinel-peridotites																
Sample:	Pra1	Pra21	Pra46	Pra68	Pra79	Pra82	Pra91	Pra94	Pra96	Pra98	Pra232	Pra233	Pra301	Pra303	Pra305	Pra306	Pra307
SiO_2	41·1	41·4	41·0	41·0	41·0	41·2	40·7	40·9	41·3	41·1	40·9	41·0	40·9	41·0	41·1	41·2	41·0
Al_2O_3	0·02	0·02	<0·02	0·04	0·03	0·04	0·04	0·04	0·03	0·03	0·03	0·03	0·02	0·04	0·02	0·02	0·04
Cr_2O_3	0·05	0·02	0·02	0·04	<0·02	<0·02	0·02	0·05	0·05	0·03	0·04	0·04	0·05	0·04	0·02	0·03	0·06
FeO*	8·7	8·2	8·8	9·0	9·1	8·5	10·1	8·6	8·1	9·0	8·9	10·1	8·4	8·2	9·5	8·8	8·1
MnO	0·14	0·13	0·13	0·15	0·14	0·12	0·18	0·13	0·13	0·12	0·16	0·15	0·13	0·11	0·14	0·14	0·16
NiO	0·38	0·47	0·45	0·34	0·33	0·41	0·35	0·38	0·36	0·38	0·35	0·37	0·45	0·38	0·45	0·41	0·39
MgO	49·9	50·7	50·1	49·7	49·5	50·4	48·4	49·7	50·4	49·4	49·8	49·2	50·1	50·3	49·9	50·3	50·5
CaO	0·08	0·04	0·07	0·13	0·07	0·09	0·10	0·11	0·11	0·08	0·13	0·08	0·15	0·13	0·06	0·07	0·17
Total	100·35	100·91	100·57	100·42	100·12	100·77	99·88	99·98	100·43	100·15	100·38	100·95	100·24	100·21	101·18	100·97	100·47
mg-no.	0·91	0·92	0·91	0·91	0·91	0·91	0·90	0·91	0·92	0·91	0·91	0·90	0·91	0·92	0·90	0·91	0·92

	Spinel–garnet peridotite												Garnet peridotites	
Sample:	Pra33	Pra38	Pra70	Pra74	Pra197	Pra198	Pra234	Pra299	Pra297	Pra399	Pra420	Pra421	Pra199	Pra302
SiO_2	41·0	41·1	41·1	41·0	40·9	40·6	41·0	40·9	41·2	40·7	41·1	41·4	41·1	41·0
Al_2O_3	0·07	0·04	0·05	0·06	0·06	0·03	0·07	0·07	<0·02	0·03	0·06	0·05	0·07	0·04
Cr_2O_3	0·06	0·04	0·06	0·01	0·01	0·03	0·06	0·08	0·03	<0·02	0·02	0·04	0·04	0·04
FeO*	9·0	9·9	8·8	9·3	8·8	9·2	8·6	9·2	9·7	10·2	10·3	9·7	10·1	10·5
MnO	0·12	0·13	0·12	0·15	0·13	0·11	0·13	0·13	0·13	0·14	0·15	0·15	0·13	0·16
NiO	0·39	0·34	0·41	0·38	0·41	0·37	0·44	0·41	0·37	0·36	0·37	0·35	0·34	0·44
MgO	49·0	48·7	49·3	49·8	50·1	49·3	50·0	49·5	49·1	48·7	48·4	49·6	49·0	48·7
CaO	0·11	0·11	0·13	0·10	0·14	0·14	0·14	0·09	0·11	0·12	0·11	0·11	0·10	0·12
Total	99·78	100·33	99·97	100·69	100·42	99·73	100·46	100·38	100·64	100·18	100·51	101·4	100·84	100·93
mg-no.	0·91	0·90	0·91	0·91	0·91	0·90	0·91	0·91	0·90	0·89	0·89	0·90	0·90	0·89

*Total Fe as FeO.

those of the olivines. Except for the outermost rim, which shows a minor decrease in Al_2O_3 content (*c.* 0·20–0·3 wt%), the orthopyroxenes are homogeneous. The Al_2O_3 concentration varies between samples by 2·9–6·1 wt% and correlates positively with the whole-rock Al_2O_3 content. On average, the Al_2O_3 content of the orthopyroxenes is higher in the garnet-bearing peridotites than in the spinel-bearing peridotites.

In both spinel–garnet-bearing lherzolites and clinopyroxene-poor lherzolites, the Al_2O_3 content of orthopyroxene is in the range 4·9–5·8 wt%, whereas in garnet-bearing lherzolites it fluctuates between 5·2 and 5·8 wt%. The Al_2O_3 content of orthopyroxene is highest in the spinel lherzolites (4·9–6·1 wt%), whereas in clinopyroxene-poor lherzolites it is in the range 2·9–4·1 wt%.

Orthopyroxenes from garnet-bearing peridotites typically have higher CaO contents than those from spinel-peridotites. In the former, CaO varies from 1·20 to 1·50 wt% and in the latter from 0·65 to 0·97 wt%. However, there are spinel-peridotites containing orthopyroxenes with higher CaO concentrations, similar to those of garnet-bearing peridotites (Table 4). Again, as in the olivine from the depleted spinel-lherzolite Pra307, the CaO content is high (1·46 wt%).

Clinopyroxene

Clinopyroxene microprobe analyses are given in Table 5. They are Cr-diopsides with compositions of $En_{50–54}$ $Wo_{39–45}Fs_{5–7}$ in the garnet-bearing peridotites and $En_{49–54}$ $Wo_{42–47}Fs_{4–6}$ in the spinel-peridotites. Like orthopyroxene, clinopyroxene grains are fairly homogeneous with the exception of the outer rims, which show a systematic minor decrease of Al_2O_3 content of the order of 0·20 and 0·30 wt%. The concentration of Al_2O_3 varies between

Table 4: Electron microprobe analyses of orthopyroxenes from Prahuaniyeu peridotite xenoliths, northern Patagonia, Argentina

	Spinel-peridotites																
Sample:	Pra1	Pra21	Pra46	Pra68	Pra79	Pra82	Pra91	Pra94	Pra96	Pra98	Pra232	Pra233	Pra301	Pra303	Pra305	Pra306	Pra307
SiO_2	55·1	55·7	55·8	55·0	54·8	55·9	54·1	55·3	55·7	55·0	54·9	54·6	56·1	55·4	56·3	55·9	55·1
TiO_2	0·15	0·03	0·04	0·03	0·04	0·01	0·22	0·04	0·06	0·26	0·12	0·19	0·01	0·03	0·08	0·10	0·05
Al_2O_3	3·8	3·8	3·9	4·9	4·9	3·5	6·1	3·7	3·8	4·7	5·4	5·5	3·4	3·4	2·9	4·1	3·3
Cr_2O_3	0·81	0·50	0·44	0·74	0·46	0·72	0·45	0·92	0·95	0·60	0·70	0·38	0·66	1·04	0·60	0·59	1·00
FeO*	5·3	5·2	5·5	5·7	5·8	5·4	6·4	5·4	5·1	5·6	5·7	6·4	5·3	5·2	6·1	5·6	5·2
MnO	0·12	0·13	0·17	0·12	0·15	0·13	0·13	0·13	0·12	0·12	0·15	0·12	0·15	0·11	0·13	0·13	0·12
NiO	0·12	0·13	0·13	0·14	0·06	0·10	0·12	0·11	0·12	0·10	0·06	0·09	0·10	0·08	0·11	0·10	0·06
MgO	33·4	34·1	34·1	32·8	33·0	34·0	31·6	33·1	33·1	32·8	32·6	32·4	34·0	33·3	34·0	33·4	33·5
CaO	0·95	0·70	0·66	1·20	0·79	0·87	1·09	1·30	1·31	0·97	1·20	0·93	0·93	1·47	0·65	0·83	1·46
Na_2O	0·14	0·10	0·08	0·15	0·17	0·08	0·19	0·11	0·14	0·09	0·15	0·16	0·02	0·08	0·11	0·08	0·08
Total	99·87	100·39	100·8	100·69	100·10	100·80	100·36	100·12	100·25	100·22	100·90	100·80	100·67	100·08	100·94	100·84	99·79
mg-no.	0·92	0·92	0·92	0·91	0·91	0·92	0·90	0·92	0·92	0·91	0·91	0·90	0·92	0·92	0·91	0·91	0·92
en	90·1	90·8	90·5	89·0	89·6	90·3	87·8	89·3	89·7	89·5	88·9	88·5	90·3	89·4	89·7	90·0	89·5
wo	1·8	1·3	1·3	2·3	1·5	1·6	2·2	2·5	2·6	1·9	2·4	1·8	1·8	2·8	1·2	1·6	2·8
fs	8·1	7·8	8·2	8·6	8·8	8·1	10·0	8·2	7·7	8·6	8·7	9·7	7·9	7·8	9·1	8·4	7·7

	Spinel–garnet-peridotites												Garnet-peridotites	
Sample:	Pra33	Pra38	Pra70	Pra74	Pra197	Pra198	Pra234	Pra299	Pra297	Pra399	Pra420	Pr421	Pra199	Pr302
SiO_2	54·1	54·2	54·4	54·5	54·9	54·0	54·7	54·9	55·9	54·3	54·5	55·0	54·2	54·8
TiO_2	0·15	0·13	0·08	0·15	0·0	0·15	0·07	0·10	0·20	0·19	0·19	0·07	0·18	0·06
Al_2O_3	5·6	5·8	5·0	5·7	4·9	5·3	4·9	4·9	3·2	5·9	5·8	5·3	5·8	5·2
Cr_2O_3	0·78	0·51	1·03	0·65	0·97	0·68	1·01	0·88	0·32	0·59	0·56	0·69	0·57	0·52
FeO*	5·6	6·2	5·6	5·8	5·6	5·6	5·5	5·6	6·6	6·5	6·5	6·0	6·2	6·3
MnO	0·13	0·14	0·09	0·10	0·12	0·13	0·12	0·12	0·14	0·12	0·11	0·14	0·13	0·14
NiO	0·09	0·13	0·08	0·13	0·11	0·10	0·16	0·11	0·12	0·11	0·09	0·11	0·10	0·12
MgO	31·4	31·5	31·4	32·4	32·6	32·1	32·6	32·7	33·4	31·6	31·7	32·3	31·4	32·3
CaO	1·28	1·20	1·42	1·21	1·49	1·29	1·52	1·50	1·21	1·21	1·22	1·24	1·26	1·25
Na_2O	0·18	0·12	0·14	0·19	0·13	0·16	0·12	0·14	0·09	0·24	0·21	0·10	0·21	0·10
Total	99·28	99·97	99·15	100·73	100·84	99·52	100·64	100·87	101·18	100·72	100·88	100·95	99·98	100·82
mg-no.	0·91	0·90	0·91	0·91	0·91	0·91	0·91	0·91	0·90	0·90	0·90	0·91	0·90	0·90
en	88·5	88·0	88·3	88·7	88·5	88·8	88·6	88·6	87·9	87·5	87·5	88·4	87·7	88·0
wo	2·6	2·4	2·9	2·4	2·9	2·6	3·0	2·9	2·3	2·4	2·4	2·4	2·5	2·5
fs	8·9	9·6	8·8	9·0	8·6	8·6	8·4	8·5	9·8	10·1	10·1	9·2	9·7	9·6

*Total Fe as FeO.

samples in the range of 3·5–8·0 wt%. Generally, Al_2O_3 contents decrease with increasing mg-number (Fig. 6). The TiO_2 contents range from 0·02 to 0·68 wt% and also decrease with increasing mg-number. The lowest TiO_2, at *c.* 0·02 wt%, was observed in the spinel-peridotite Pra82.

Spinel

Spinel microprobe analyses are given in Table 6. All analyzed spinels lack chemical zonation and they are homogeneous in composition within each sample. Spinels in the spinel–garnet-peridotites are relatively Cr poor, with cr-number $[Cr/(Cr+Al+Fe^{3+})]$ varying within the

Table 5: Electron microprobe analyses of clinopyroxenes from Prahuaniyeu peridotite xenoliths, northern Patagonia, Argentina

	Spinel-peridotites																
Sample:	Pra1	Pra21	Pra46	Pra68	Pra79	Pra82	Pra91	Pra94	Pra96	Pra98	Pra232	Pra233	Pra301	Pra303	Pra305	Pra306	Pra307
SiO_2	52·9	53·2	52·7	52·9	52·7	53·0	51·6	52·8	53·1	51·9	52·4	52·0	53·2	53·0	53·7	52·8	52·5
TiO_2	0·31	0·08	0·10	0·08	0·23	0·00	0·67	0·08	0·06	0·63	0·29	0·68	0·04	0·10	0·15	0·29	0·07
Al_2O_3	4·8	4·6	4·9	5·5	6·3	4·0	8·0	4·3	4·2	5·9	6·2	7·6	3·5	3·7	4·5	5·5	3·6
Cr_2O_3	1·50	0·97	0·86	1·26	0·77	1·29	0·73	1·53	1·52	1·13	1·06	0·70	1·11	1·51	1·39	1·22	1·46
FeO*	2·44	2·33	2·36	3·0	2·7	2·5	3·4	2·9	2·7	2·5	2·8	3·3	2·26	2·8	2·8	2·7	2·9
MnO	0·09	0·11	0·07	0·10	0·07	0·08	0·09	0·10	0·09	0·06	0·10	0·11	0·07	0·11	0·08	0·09	0·08
NiO	0·06	0·03	0·06	0·06	0·03	0·10	0·06	0·05	0·05	0·04	0·08	0·02	0·04	0·06	0·05	0·02	0·03
MgO	16·4	16·2	16·6	17·1	15·7	17·2	15·6	17·8	17·5	16·4	17·1	15·2	17·7	18·0	15·8	15·9	18·4
CaO	20·0	21·2	21·8	19·3	20·4	21·1	18·3	19·8	19·8	20·6	19·6	18·8	22·2	19·7	20·7	20·6	19·9
Na_2O	1·42	1·30	1·47	1·29	1·55	0·93	1·68	0·91	1·02	1·09	1·10	1·91	0·47	0·81	1·60	1·46	0·65
Total	99·96	100·00	100·86	100·47	100·46	100·14	100·08	100·24	100·01	100·26	100·70	100·26	100·50	99·77	100·78	100·59	99·51
mg-no.	0·92	0·93	0·93	0·91	0·91	0·92	0·89	0·92	0·92	0·92	0·92	0·89	0·93	0·92	0·91	0·91	0·92
en	51·0	49·4	49·4	52·4	49·3	51·0	51·0	52·9	52·6	50·3	52·2	49·7	50·6	53·4	49·0	49·3	53·6
wo	44·7	46·6	46·6	42·5	46·0	44·9	42·9	42·2	42·9	45·3	42·9	44·2	45·7	42·0	46·0	46·1	41·7
fs	4·3	4·0	3·9	5·1	4·7	4·1	6·1	4·8	4·5	4·4	4·8	6·1	3·6	4·6	4·9	4·6	4·7

	Spinel–garnet-peridotites												Garnet-peridotites	
Sample:	Pra33	Pra38	Pra70	Pra74	Pra197	Pra198	Pra234	Pra297	Pra299	Pra399	Pra420	Pra421	Pra199	Pra302
SiO_2	52·2	52·4	52·2	51·9	52·3	52·2	52·5	52·5	52·4	51·9	51·9	52·6	51·9	52·7
TiO_2	0·37	0·30	0·18	0·46	0·10	0·25	0·08	0·27	0·17	0·61	0·58	0·15	0·66	0·13
Al_2O_3	6·8	6·5	5·7	7·0	5·6	6·3	5·2	6·4	5·5	7·5	7·7	6·1	7·5	5·8
Cr_2O_3	1·27	0·90	1·49	1·08	1·39	1·07	1·38	0·99	1·36	0·92	0·90	1·03	1·09	0·72
FeO*	3·3	3·0	3·2	3·3	3·4	2·9	3·0	3·1	3·1	3·7	3·8	3·1	3·8	3·3
MnO	0·13	0·11	0·10	0·10	0·10	0·10	0·10	0·13	0·08	0·11	0·11	·09	0·13	0·13
NiO	0·05	0·05	0·08	0·04	0·10	0·08	0·05	0·06	0·05	0·06	0·06	0·05	0·01	0·07
MgO	16·3	16·0	17·0	17·1	17·7	16·7	18·1	16·8	17·7	16·0	16·1	16·9	16·5	17·3
CaO	18·0	19·9	18·3	17·5	18·9	19·1	19·2	19·5	18·3	17·1	17·5	19·6	16·8	20·1
Na_2O	1·42	1·19	1·05	1·46	0·91	1·33	0·72	1·11	1·15	2·11	1·70	0·96	1·78	0·80
Total	99·69	100·36	99·18	99·89	100·49	100·06	100·34	100·86	99·77	99·94	100·35	100·53	100·22	100·96
mg-no.	0·90	0·90	0·91	0·90	0·90	0·91	0·92	0·91	0·91	0·89	0·88	0·91	0·89	0·90
en	52·5	50·0	53·3	54·3	53·4	52·0	53·9	51·6	54·4	52·8	52·3	51·6	53·8	51·5
wo	41·6	44·7	41·1	39·9	40·9	42·9	41·1	43·1	40·2	40·5	40·8	43·1	39·3	43·1
fs	5·9	5·3	5·6	5·9	5·7	5·1	5·0	5·3	5·3	6·8	6·9	5·3	6·9	5·5

*Total Fe as FeO.

narrow range of 0·12–0·28. On the other hand, spinels in the spinel-peridotites vary from Cr poor (cr-number = 0·09) to Cr-rich (cr-number = 0·47). Coexisting spinels and olivines plot within the OSMA field of Arai (1994) and define a linear trend with overlapping spinel–garnet-peridotites and spinel-peridotites in the most Al-rich part of the field (Fig. 7).

Garnet

Garnet microprobe analyses are given in Table 7. Like spinels, garnets lack chemical zonation and are homogeneous within samples. There are no significant compositional differences between those in spinel–garnet- and in garnet-bearing peridotites ($Alm_{11-12}Py_{71-74}Spess_{0·5-0·6}Gross_{12-15}$). The Cr_2O_3 contents vary between 1·21 and 3·02 wt%.

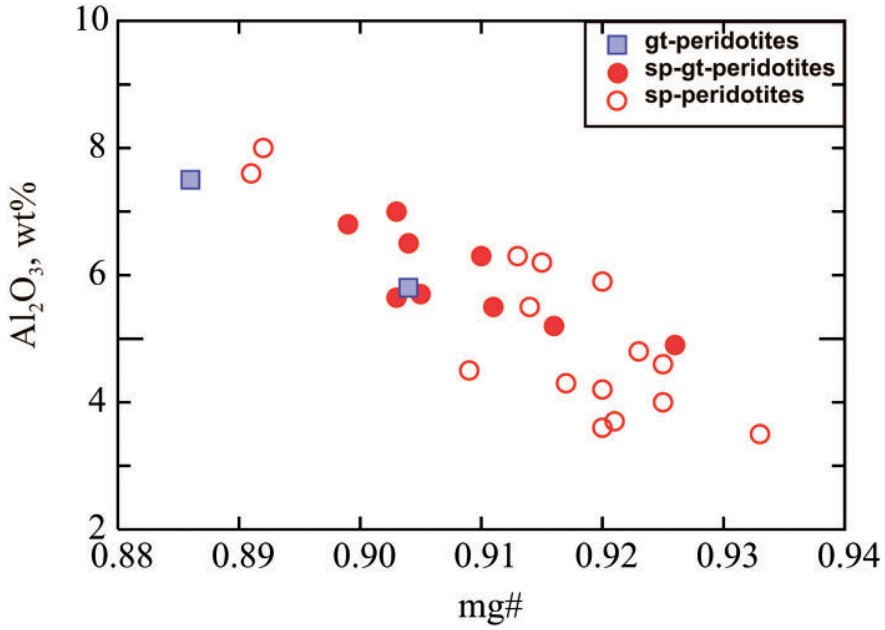

Fig. 6. Variation of clinopyroxene Al_2O_3 contents with mg-number.

Low Cr_2O_3 garnets are found in the most fertile peridotites Pral99 and Pra302. However, the lowest Cr_2O_3 content was found in garnets from sample Pra38 (Cr_2O_3 1·14 wt%). Because of its small size, this sample was not analyzed for bulk major and trace elements. Judging from its mineral compositions (Fo_{90}; cr-number = 0·12; 6·5 and 5·8 wt% Al_2O_3 in clinopyroxene and orthopyroxene, respectively) this spinel–garnet-bearing peridotite is fertile.

Trace elements

In situ trace element analyses were performed only on clinopyroxene and garnet, as olivine and orthopyroxene have low concentrations very close to the detection limits of the LA-ICP-MS method.

Clinopyroxenes

Clinopyroxene trace element analyses are given in Table 8. Clinopyroxenes from the garnet-bearing peridotites (Pral99 and Pra302) and from spinel–garnet-peridotites (Pra33, Pra38, Pra74, Pral98, Pra299 and Pra399) are characterized by a wide variation of Sr and Zr contents, ranging from 0·10 to 125 ppm and from 0·10 to 23 ppm, respectively. Similarly, the REE also show a wide compositional range. In particular, Ce varies from 0·01 to 8·01 ppm and Yb from 0·05 to 0·62 ppm. These variations can be seen in the Primitive Mantle normalized REE patterns (Fig. 8). Samples Pra33, Pra74, Pra399 (Fig. 8c) and Pral99 (Fig. 8a) have convex-upward REE patterns with $(Ce/Yb)_{PM} = 3·4–7·2$. Samples Pral98 and Pra302 show an overall depletion in REE compared with samples Pra33, Pra74, Pral99 and Pra399. Their $(Ce/Yb)_{PM}$ ranges from 0·3 to 2·4 and they show LREE depletion [$(Ce/Sm)_{PM} = 0·1–0·3$], with the exception of La and Ce, which show an enrichment relative to the other LREE. Sample Pra70 (Fig. 8e) is enriched in LREE and depleted in HREE [$(Ce/Yb)_{PM} = 6·6$] in contrast to sample Pra38 (Fig. 8e), which has a convex-upward pattern and the highest concentration in HREE. Sample Pra299 (Fig. 8e) shows a flat MREE–HREE pattern, whereas the LREE are strongly depleted with variable La and Ce enrichments relative to the other LREE. All samples have a negative Zr-anomaly (Fig. 8b, d and f). This anomaly correlates positively with the degree of HREE depletion. A similar trend can be seen for Sr, although not as well defined as for Zr. The stronger the overall REE depletion, the higher the negative Sr-anomaly. With the exception of sample Pra299, which shows a positive Ti-anomaly (Fig. 8f), none of the samples show any significant positive or negative Ti-anomaly.

Primitive mantle-normalized REE and trace element patterns for clinopyroxenes from spinel-peridotites are shown in Fig. 9. Except for the cpx from sample Pra79 (Fig. 9a), which is depleted in LREE, all the other samples have cpx REE patterns showing variably high LREE, with $(La/Sm)_{PM}$ ratios ranging between 0·5 and 10·1.

On the basis of their REE patterns, the clinopyroxenes can be divided into four groups. Group 1 (Fig. 9a), comprising samples Pra304 and Pra79, has REE that decrease

Table 6: Electron microprobe analyses of spinel from Prahuaniyeu peridotite xenoliths, northern Patagonia, Argentina

	Spinel-peridotites															
Sample:	Pra1	Pra21	Pra46	Pra79	Pra82	Pra91	Pra94	Pra96	Pra98	Pra232	Pra233	Pra301	Pra303	Pra305	Pra306	Pra307
SiO_2	0·06	0·07	0·05	0·07	0·07	0·11	0·15	0·13	0·08	0·14	0·10	0·02	0·10	0·04	0·07	0·12
TiO_2	0·36	0·01	0·03	0·09	0·05	0·23	0·13	0·15	0·36	0·24	0·24	0·05	0·20	0·19	0·21	0·17
Al_2O_3	39·5	47·9	51·8	56·1	38·6	58·4	33·3	32·3	49·2	51·1	56·9	39·5	28·4	36·9	46·8	28·1
Cr_2O_3	29·3	20·2	17·4	11·7	29·9	8·5	35·1	36·5	19·6	16·9	9·0	29·6	40·3	29·4	20·6	39·8
Fe_2O_3	1·15	2·24	1·46	1·72	2·39	1·55	2·5	2·6	0·47	1·69	3·7	1·89	2·8	4·2	2·7	3·6
FeO	10·0	8·8	9·1	8·8	9·6	9·1	10·9	10·5	9·6	8·4	8·0	9·1	10·4	11·4	9·4	9·8
MnO	0·05	0·04	0·04	0·12	0·05	0·06	0·07	0·06	0·07	0·03	0·11	0·06	0·08	0·07	0·08	0·05
NiO	0·24	0·38	0·43	0·37	0·27	0·36	0·24	0·23	0·31	0·27	0·42	0·23	0·15	0·25	0·28	0·24
MgO	18·4	19·8	20·2	20·7	18·3	20·7	17·1	17·3	19·6	20·7	21·4	18·8	17·0	17·1	19·5	17·2
Total	98·97	99·46	100·55	99·60	99·19	99·04	99·57	99·81	99·28	99·44	99·83	99·23	99·51	99·51	99·58	99·17
cr-no.	0·33	0·22	0·18	0·12	0·33	0·09	0·40	0·42	0·21	0·18	0·09	0·33	0·47	0·33	0·22	0·47

	Spinel–garnet-peridotites											
Sample:	Pra33	Pra38	Pra70	Pra74	Pra197	Pra198	Pra234	Pra297	Pra299	Pra399	Pra420	Pra421
SiO_2	0·13	0·10	0·15	0·15	0·14	0·12	0·20	0·09	0·11	0·13	0·11	0·10
TiO_2	0·32	0·17	0·27	0·30	0·26	0·07	0·19	0·16	0·21	0·40	0·35	0·15
Al_2O_3	48·9	55·8	42·5	50·5	56·7	51·2	44·3	53·0	58·6	52·5	54·5	51·3
Cr_2O_3	18·1	12·0	24·8	17·2	10·7	16·7	22·9	14·9	8·7	12·8	11·7	17·2
Fe_2O_3	2·10	0·92	2·19	2·7	2·16	2·30	3·4	2·13	1·67	3·8	3·3	1·97
FeO	9·1	9·3	10·7	8·4	9·0	8·0	9·1	8·7	8·1	8·8	9·3	9·1
MnO	0·07	0·06	0·05	0·15	0·09	0·08	0·10	0·10	0·12	0·05	0·10	0·09
NiO	0·37	0·38	0·31	0·34	0·16	0·36	0·32	0·34	0·10	0·43	0·34	0·31
MgO	19·8	20·3	18·2	20·7	21·1	20·7	19·5	20·6	21·6	20·4	20·5	20·3
Total	98·86	99·00	99·19	100·45	100·22	99·46	100·08	100·02	99·19	99·34	100·2	100·52
cr-no.	0·19	0·12	0·28	0·18	0·11	0·18	0·25	0·15	0·09	0·13	0·12	0·18

smoothly from Lu to Nd. In sample Pra304 they then increase rapidly from Nd to La $[(La/Nd)_{PM} = 8–12]$ whereas in Pra79 the LREE continue to decrease $[(La/Nd)_{PM} = 0·18–0·30]$. Group 2 (Fig. 9c) has U-shaped REE patterns, with a minimum at Eu and Gd (Pra2l and Pra30l). Group 3 (Fig. 9e) has relatively flat REE patterns, varying from 1 × PM to 3 × PM; samples Pra1 and Pra68 have convex-upward LREE patterns. Group 4 (Fig. 9g), which comprises samples Pra82 and Pra307, has the highest LREE enrichments $[(La/Yb)_{PM} = 13·4–18·0]$, and REE abundances decrease smoothly from La to Lu. In the primitive mantle-normalized multi-element diagrams, the clinopyroxenes from groups 1 and 2 have a positive Sr-anomaly and a negative Ti-anomaly, except for sample Pra30l, which has a positive Ti-anomaly (Fig. 9b and d). A pronounced Zr-anomaly has been observed only in clinopyroxenes from samples Pra30l and Pra304. In group 3, characterized by relatively flat REE patterns, clinopyroxenes have weak or no Zr- and Ti-anomalies (Fig. 9e and f). The clinopyroxenes in samples Pra82 and Pra307 (Fig. 9g and h) from group 4, with the highest enrichment in LREE [(7–15) × PM], have the most pronounced negative Ti-anomaly and the highest enrichment in Th and U of all the analyzed clinopyroxenes.

Garnets

Garnet trace element analyses are given in Table 9. They typically show strong LREE depletion [~0·003–0·03) × PM] and HREE enrichments that vary from ~9 × PM to 50 × PM (Fig. 10a and c). In their primitive-mantle normalized multi-element patterns, all garnets have strong negative Sr-anomalies relative to Pr and Nd and, except for garnets from sample Pra299, negative Ti-anomalies relative to Eu and Gd. Zirconium contents in

garnets vary from 0·21 to 0·65 ppm. Garnets depleted in REE, such as sample Pra299, have negative Zr-anomalies compared with Nd and Sm in the primitive-mantle normalized multi-element diagrams, whereas garnets with high REE contents, which correspond to fertile peridotites, have positive Zr-anomalies (Pra33, Pra74, Pra199 and Pra399, Fig. 10b and d). A core-to-rim traverse across a garnet from sample Pra199 shows systematic trace element zoning, with the core enriched in REE and other trace elements relative to the rim. The core has a REE pattern with high HREE (Yb_{PM} ~20 × PM) and the rim has low HREE (Yb_{PM} ~10 × PM). The HREE zonation, as can be seen in Table 9, is consistent with the high Zr concentration in the core (Zr 65 ppm) and low Zr concentrations in the rim (Zr 37 ppm).

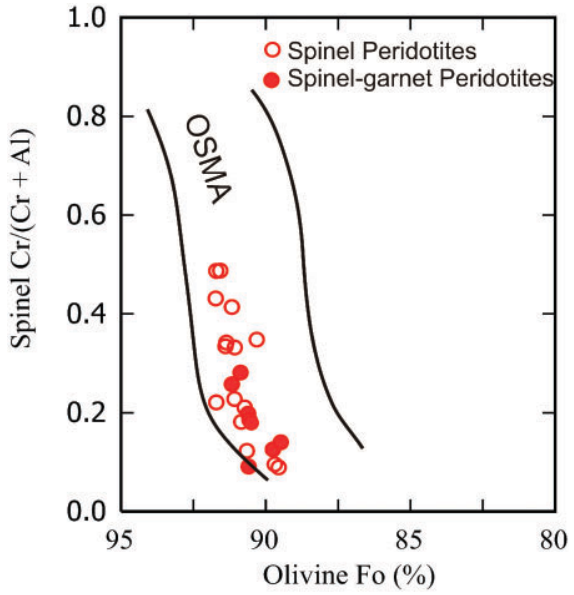

Fig. 7. Distribution of spinel–olivine pairs from the Prahuaniyeu peridotites on the spinel cr-number vs olivine Fo% diagram, showing the olivine–spinel mantle array (OSMA) defined by Arai (1994). The spinels from the garnet–spinel-peridotites are characterized by high Al_2O_3 contents.

Radiogenic isotopes

The whole-rock Nd isotope composition was determined for the garnet-peridotite Pra199. In addition, Nd-isotope compositions were measured on separates of clinopyroxene, orthopyroxene and garnet from the garnet-peridotites Pra199 and spinel–garnet-peridotite Pra74 and clinopyroxene from the spinel-peridotite Pra1 (Table 10). Clinopyroxenes from the garnet-peridotites Pra199 and Pra74 have $^{143}Nd/^{144}Nd$ ratios of 0·513158 and 0·513144, respectively; these are approximately the same as the ratios of the end-member depleted mantle component DMM (Zindler & Hart, 1986). Clinopyroxene from the spinel-peridotite Pra1 is more radiogenic ($^{143}Nd/^{144}Nd = 0·512637$) than those from the garnet-peridotites and approximates the end-member component Bulk Silicate Earth (BSE). Model ages for the two garnet-bearing samples Pra199 and Pra74 indicate apparent

Table 7: Electron microprobe analyses of garnets from Prahuaniyeu peridotite xenoliths, northern Patagonia, Argentina

	Spinel–garnet-peridotites												Garnet-peridotites	
Sample:	Pra33	Pra38	Pra70	Pra74	Pra197	Pra198	Pra234	Pra297	Pra299	Pra399	Pra420	Pra421	Pra199	Pra302
SiO_2	42·4	42·3	42·1	42·0	41·9	42·7	42·7	42·5	42·6	42·3	42·6	42·7	42·6	42·2
TiO_2	0·21	0·14	0·19	0·23	0·10	0·11	0·08	0·14	0·13	0·26	0·26	0·14	0·29	0·09
Al_2O_3	23·0	23·4	22·2	23·2	22·2	23·0	22·0	22·5	22·4	23·1	23·2	22·8	23·2	23·3
Cr_2O_3	1·68	1·14	2·6	1·31	2·9	1·45	3·02	1·46	2·6	1·06	1·04	1·47	1·27	1·21
FeO	6·4	7·0	6·1	6·4	6·2	6·3	5·8	6·8	6·1	7·5	7·3	6·7	7·0	7·1
MnO	0·25	0·32	0·26	0·33	0·26	0·29	0·26	0·29	0·28	0·32	0·30	0·32	0·28	0·29
NiO	<0·02	0·04	<0·02	0·03	0·03	0·02	<0·02	<0·02	0·03	<0·02	<0·02	<0·02	0·00	0·00
MgO	21·4	20·8	20·9	21·1	20·4	21·3	21·0	22·5	21·0	20·4	21·2	21·0	21·3	20·3
CaO	5·3	5·5	5·6	5·2	6·1	5·6	6·1	5·6	5·8	5·1	5·0	5·6	5·0	5·8
Na_2O	0·02	0·02	0·02	<0·02	<0·02	0·02	0·02	0·02	<0·02	<0·02	<0·02	<0·02	0·03	0·02
Total	100·60	100·64	99·96	99·79	100·09	100·76	100·98	100·48	100·86	100·06	100·90	100·73	100·90	100·36
alm	12·0	13·2	11·9	12·3	12·3	11·6	10·9	11·2	11·6	14·9	13·1	12·2	13·0	13·9
py	74·3	72·5	73·4	74·0	71·8	73·9	73·3	74·1	73·4	71·5	73·8	73·1	74·1	71·0
spes	0·5	0·6	0·5	0·7	0·5	0·6	0·5	0·6	0·6	0·6	0·6	0·6	0·5	0·6
gros	13·2	13·7	14·2	13·0	15·4	13·9	15·3	10·6	14·5	13·1	12·3	13·8	12·4	14·6

Table 8: LA-ICP-MS analyses, in ppm, of clinopyroxenes from Prahuaniyeu peridotite xenoliths, northern Patagonia, Argentina

	Spinel-peridotites																					
Sample:	Pra1	Pra1	Pra1	Pra21	Pra21	Pra21	Pra21	Pra21	Pra48	Pra48	Pra48	Pra48	Pra68	Pra68	Pra68	Pra68	Pra79	Pra79c	Pra79r	Pra79c	Pra79r	Pra82
Sc	63·0	64·1	56·0	64·0	57·0	70·3	60·5	58·0	40·7	39·3	40·6	45·1	72·0	60·7	48·3	49·4	55·6	58·5	54·7	52·4	51·7	58·8
V	195	194	191	150	144	143	150	134	167	165	175	166	185	186	190	188	211	224	235	207	217	193
Co	22·2	20·7	23·3	20·7	21·4	19·7	19·6	18·3	23·1	23·5	22·9	22·4	20·7	19·3	21·8	20·5	21·2	23·3	23·1	21·0	22·7	19·8
Rb	0·01	0·01	<0·01	0·02	0·02	0·01	0·01	0·02	0·01	0·01	0·02	0·01	<0·01	0·01	<0·01	0·02	0·02	0·02	0·01	0·01	0·05	<0·01
Sr	107	116	114	129	133	130	140	132	12·9	13·2	13·7	12·5	101	99·2	107	101	13·8	15·4	14·4	14·2	14·9	132
Y	4·36	4·76	4·30	3·67	4·44	3·91	3·95	4·34	3·37	2·97	3·15	3·33	4·36	4·03	3·93	3·84	13·2	13·7	13·1	12·3	12·4	3·35
Zr	17·4	19·7	17·6	5·65	6·71	6·19	5·07	6·33	2·44	2·25	2·31	2·23	18·7	17·1	16·2	16·1	6·89	7·08	6·37	6·33	6·44	33·9
Nb	0·09	0·47	0·46	0·67	0·71	0·57	0·75	0·66	0·27	0·28	0·24	0·25	0·51	0·42	0·41	0·49	0·11	0·13	0·15	0·14	0·20	2·99
Ba	1·29	0·11	0·12	0·05	0·09	0·09	0·11	0·06	1·05	1·26	1·98	0·94	0·19	0·06	0·08	0·12	0·05	<0·02	0·02	0·02	0·14	0·26
La	5·06	1·43	1·38	3·04	3·08	3·08	3·14	3·22	0·55	0·49	0·51	0·50	1·18	1·09	1·18	1·12	0·05	0·07	0·05	0·05	0·09	8·83
Ce	0·97	5·61	5·70	3·68	3·59	3·60	4·09	3·69	1·38	1·33	1·39	1·24	4·22	4·52	4·83	4·62	0·21	0·23	0·23	0·23	0·25	14·74
Pr	4·99	1·03	1·08	0·35	0·40	0·40	0·40	0·42	0·21	0·18	0·18	0·17	0·77	0·82	0·84	0·81	0·06	0·07	0·07	0·06	0·07	1·77
Nd	1·43	5·31	5·40	1·55	1·65	1·38	1·46	1·40	0·93	0·77	0·93	0·82	4·47	4·16	4·62	4·36	0·53	0·57	0·54	0·56	0·60	8·63
Sm	0·56	1·47	1·52	0·27	0·32	0·32	0·29	0·32	0·29	0·25	0·28	0·26	1·07	1·34	1·31	1·25	0·53	0·51	0·52	0·53	0·58	1·56
Eu	0·14	0·56	0·53	0·11	0·12	0·12	0·12	0·13	0·07	0·07	0·08	0·07	0·43	0·49	0·44	0·43	0·30	0·31	0·31	0·32	0·29	0·51
Tb	1·15	0·15	0·15	0·07	0·07	0·07	0·07	0·07	0·07	0·07	0·06	0·05	0·13	0·14	0·12	0·16	0·26	0·25	0·25	0·24	0·26	0·16
Gd	0·83	1·32	1·12	0·38	0·36	0·40	0·30	0·30	0·30	0·31	0·28	0·29	1·16	1·10	1·03	0·97	1·20	1·18	1·19	1·17	1·22	1·21
Dy	0·19	0·76	0·72	0·48	0·51	0·58	0·52	0·55	0·57	0·50	0·49	0·53	0·89	0·80	0·72	0·63	2·05	1·98	2·18	2·09	1·99	0·75
Ho	0·48	0·20	0·16	0·13	0·16	0·15	0·16	0·13	0·11	0·10	0·09	0·12	0·13	0·15	0·15	0·15	0·51	0·53	0·52	0·49	0·50	0·15
Er	0·09	0·51	0·47	0·57	0·58	0·47	0·52	0·63	0·36	0·37	0·33	0·37	0·44	0·44	0·40	0·43	1·52	1·54	1·48	1·50	1·47	0·40
Tm	0·56	0·11	0·09	0·09	0·09	0·09	0·11	0·08	0·07	0·06	0·06	0·06	0·07	0·07	0·07	0·06	0·22	0·23	0·20	0·21	0·22	0·05
Yb	0·08	0·57	0·51	0·58	0·55	0·52	0·56	0·61	0·47	0·49	0·52	0·51	0·39	0·48	0·45	0·37	1·39	1·41	1·46	1·49	1·44	0·40
Lu	0·50	0·09	0·08	0·09	0·09	0·10	0·10	0·11	0·07	0·06	0·06	0·06	0·06	0·06	0·08	0·06	0·21	0·21	0·18	0·20	0·19	0·05
Hf	0·03	0·39	0·56	0·13	0·17	0·13	0·15	0·15	0·06	0·06	0·06	0·07	0·41	0·40	0·43	0·40	0·26	0·24	0·28	0·28	0·24	0·43
Ta	0·05	0·03	0·03	0·02	0·01	0·02	0·02	0·02	0·02	0·02	0·02	0·02	0·02	0·03	0·04	0·03	<0·01	<0·01	<0·01	<0·01	<0·01	0·33
Th	0·01	0·03	0·04	0·27	0·22	0·28	0·30	0·31	0·02	0·03	0·03	0·03	0·04	0·05	0·03	0·03	0·02	0·01	0·02	0·01	0·01	0·78
U	0·09	0·01	0·02	0·10	0·11	0·09	0·11	0·08	0·01	0·01	0·01	0·01	0·00	0·01	0·02	0·02	0·01	0·01	0·01	0·01	0·01	0·20

(continued)

Table 8: Continued

	Spinel-peridotites																					
Sample:	Pra82	Pra82	Pra82	Pra82	Pra87	Pra87r	Pra87c	Pra87c	Pra98r	Pra98r	Pra98	Pra98	Pra98	Pra233	Pra233c	Pra233r	Pra233c	Pra301	Pra301	Pra301	Pra301	Pra301	Pra301
Sc	61·0	54·2	60·5	62·7	55·8	58·7	60·3	59·5	60·8	60·1	60·9	59·7	58·7	58·1	58·8	58·8	56·0	49·2	47·6	47·5	46·8	45·3	45·6
V	191	180	187	183	195	198	194	188	232	236	229	228	234	295	313	295	319	155	153	164	161	175	171
Co	22·7	23·2	22·4	20·3	18·3	19·0	18·9	18·1	22·4	22·0	20·7	20·2	20·7	25·4	26·4	27·7	29·0	18·4	17·9	18·5	18·4	19·9	19·4
Rb	<0·01	0·02	<0·01	0·03	<0·01	0·01	0·01	0·01	0·01	0·01	<0·01	<0·01	0·01	0·01	0·01	0·02	0·02	0·01	0·01	0·06	<0·01	<0·01	<0·01
Sr	132	131	132	130	21·3	21·8	22·1	22·2	89·7	89·5	83·5	83·4	83·1	86·5	102	108	98·8	46·5	43·5	46·9	43·7	44·7	45·2
Y	3·52	3·14	3·27	3·35	7·03	7·80	8·47	8·52	11·4	10·2	10·1	9·52	9·39	14·6	14·0	18·9	16·4	1·53	1·39	1·56	1·51	1·40	1·47
Zr	32·2	33·4	34·0	35·2	20·2	21·2	22·4	20·9	31·2	29·3	28·9	26·6	26·8	29·0	27·5	35·2	30·9	0·19	0·16	0·14	0·14	0·18	0·17
Nb	3·06	2·87	2·77	2·81	0·18	0·19	0·21	0·20	1·07	1·02	0·93	0·94	0·89	1·93	2·20	2·52	1·91	0·16	0·17	0·17	0·16	0·16	0·17
Ba	0·27	0·38	0·26	0·25	0·05	0·04	0·07	0·02	0·02	0·06	<0·02	0·05	0·09	0·07	0·04	0·04	0·06	0·03	0·11	0·00	0·08	0·07	0·09
La	8·7	8·84	8·8	8·66	0·92	0·97	0·95	0·96	2·05	1·92	1·75	1·7	1·86	1·85	2·11	1·83	2·02	0·77	0·68	0·86	0·71	0·71	0·69
Ce	14·34	14·34	14·74	13·85	2·56	2·62	2·72	2·6	6·05	5·86	5·56	5·51	5·48	6·26	7·34	7·10	7·27	1·80	1·61	1·86	1·62	1·69	1·74
Pr	1·73	1·94	1·87	1·89	0·34	0·34	0·37	0·36	1·04	0·93	0·87	0·89	0·87	0·90	1·18	1·19	1·02	0·20	0·18	0·19	0·17	0·18	0·21
Nd	8·04	8·74	7·76	8·11	1·77	1·67	1·75	1·76	6·17	5·77	4·88	4·82	4·49	4·60	5·41	5·39	5·40	0·61	0·53	0·54	0·45	0·57	0·56
Sm	1·72	1·58	1·66	1·62	0·57	0·54	0·53	0·57	1·85	1·63	1·55	1·62	1·48	1·56	1·70	1·63	1·81	0·05	0·04	0·05	0·05	0·04	0·04
Eu	0·49	0·52	0·5	0·51	0·22	0·24	0·24	0·25	0·65	0·65	0·61	0·58	0·58	0·66	0·71	0·77	0·75	0·01	0·01	0·01	0·01	0·01	0·01
Tb	0·15	0·17	0·15	0·16	0·14	0·15	0·14	0·16	0·34	0·3	0·3	0·32	0·29	0·38	0·34	0·41	0·41	0·01	0·01	0·01	0·01	0·01	0·01
Gd	1·18	1·19	1·17	1·2	0·73	0·76	0·82	0·78	1·84	1·86	1·8	1·66	1·75	1·99	2·00	2·11	2·18	0·04	0·04	0·04	0·04	0·04	0·04
Dy	0·74	0·82	0·8	0·87	1·19	1·21	1·37	1·2	2·18	2·01	1·92	1·78	1·84	2·60	2·49	2·36	2·73	0·17	0·14	0·14	0·13	0·15	0·15
Ho	0·14	0·16	0·15	0·14	0·27	0·29	0·28	0·27	0·44	0·4	0·39	0·4	0·35	0·56	0·51	0·51	0·58	0·05	0·04	0·05	0·04	0·05	0·04
Er	0·3	0·35	0·33	0·35	0·82	0·79	0·91	0·85	1·18	1·11	1·08	0·87	1	1·50	1·48	1·54	1·51	0·19	0·17	0·19	0·16	0·17	0·17
Tm	0·05	0·05	0·05	0·05	0·13	0·13	0·14	0·13	0·18	0·13	0·14	0·15	0·13	0·22	0·20	0·24	0·26	0·04	0·03	0·03	0·03	0·03	0·03
Yb	0·32	0·38	0·33	0·37	0·88	0·95	0·98	0·96	1·08	0·89	1·02	0·89	0·85	1·54	1·39	1·48	1·51	0·29	0·28	0·30	0·28	0·27	0·28
Lu	0·06	0·06	0·05	0·06	0·11	0·11	0·13	0·13	0·17	0·15	0·13	0·13	0·12	0·20	0·20	0·22	0·22	0·05	0·05	0·05	0·05	0·05	0·05
Hf	0·31	0·33	0·32	0·46	0·3	0·28	0·25	0·27	1·12	1·02	0·98	0·97	0·94	0·81	0·75	0·91	0·81	0·01	0·01	0·01	0·01	0·01	0·01
Ta	0·35	0·37	0·25	0·37	0·01	<0·01	<0·01	<0·01	0·13	0·12	0·1	0·1	0·12	0·12	0·12	0·13	0·12	0·01	0·01	0·01	0·01	0·01	0·01
Th	0·72	0·68	0·83	0·67	0·05	0·07	0·07	0·07	0·11	0·11	0·1	0·11	0·12	0·18	0·25	0·29	0·16	0·02	0·04	0·04	0·04	0·04	0·03
U	0·16	0·14	0·18	0·15	0·01	0·01	0·01	0·01	0·04	0·03	0·03	0·03	0·03	0·08	0·09	0·10	0·10	0·01	0·01	0·01	0·01	0·01	0·01

(continued)

Table 8: Continued

	Spinel-peridotites						Spinel–garnet-peridotites														
Sample:	Pra304c	Pra304r	Pra304	Pra307	Pra307c	Pra307r	Pra33	Pra33	Pra33	Pra38	Pra38	Pra70c	Pra74	Pra74	Pra74	Pra74	Pra198	Pra198r	Pra198	Pra299	Pra299
Sc	59·8	60·9	55·9	40·1	42·4	43·7	32·7	30·8	29·7	36·1	35·1	26·5	41·6	37·7	38·6	38·1	27·5	27·0	22·4	19·4	21·7
V	210	230	225	140	136	138	241	263	261	163	163	248	190	180	192	211	182	197	193	173	231
Co	20·3	20·2	20·1	25·8	27·0	27·1	28·9	31·8	32·0	22·3	21·7	29·7	28·1	25·2	24·2	25·7	20·6	23·5	23·2	23·9	29·2
Rb	<0·01	0·01	0·01	0·01	<0·01	<0·01	0·01	0·01	0·01	0·01	0·01	0·01	0·01	<0·01	<0·01	0·01	0·03	0·03	0·12	0·02	0·01
Sr	16·6	21·3	12·2	76·7	83·5	74·0	76·34	75·13	76·80	5·99	5·51	32·5	75·7	75·8	75·6	72·4	7·48	7·13	8·35	0·21	0·24
Y	11·1	10·2	8·97	1·92	2·10	2·26	5·35	5·07	5·14	8·55	7·53	1·99	6·55	7·18	5·77	5·52	3·04	3·04	2·81	1·32	1·19
Zr	0·69	0·68	0·63	5·79	6·47	6·50	13·5	13·5	12·5	3·22	2·86	3·83	15·7	18·5	15·4	14·5	1·13	1·36	1·26	0·12	0·08
Nb	0·18	0·20	0·18	0·56	0·58	0·56	0·46	0·53	0·55	0·22	0·18	0·76	0·28	0·33	0·27	0·23	0·33	0·36	0·30	0·11	0·10
Ba	0·03	0·04	0·03	0·97	0·59	0·79	0·24	0·21	1·01	0·83	0·26	0·19	0·21	0·13	0·22	0·29	2·27	2·63	2·52	0·90	0·79
La	2·14	2·33	1·65	3·72	4·25	4·41	1·53	1·59	0·13	0·13	1·65	1·44	1·18	1·09	1·01	1·02	0·57	0·55	0·56	0·02	0·02
Ce	2·05	2·79	2·00	6·97	7·94	7·68	6·02	6·19	0·35	0·28	3·58	3·06	3·90	3·82	3·86	3·76	1·01	0·92	0·94	0·01	0·02
Pr	0·09	0·18	0·13	0·71	0·86	0·84	0·84	0·80	0·10	0·11	0·39	0·35	0·70	0·74	0·68	0·69	0·14	0·14	0·13	0·00	0·00
Nd	0·35	0·44	0·41	2·82	3·52	3·54	3·58	3·64	0·93	0·85	1·59	1·57	3·71	4·26	3·58	3·69	0·89	1·01	0·91	0·04	0·05
Sm	0·37	0·25	0·30	0·55	0·60	0·56	1·05	1·17	0·83	0·77	0·48	0·44	1·31	1·35	1·28	1·26	0·64	0·66	0·64	0·11	0·14
Eu	0·17	0·18	0·17	0·19	0·18	0·19	0·42	0·45	0·43	0·33	0·18	0·18	0·53	0·52	0·53	0·52	0·26	0·28	0·27	0·07	0·07
Tb	0·19	0·17	0·17	0·09	0·10	0·09	0·18	0·19	0·28	0·22	0·08	0·09	0·26	0·27	0·24	0·25	0·15	0·14	0·15	0·05	0·05
Gd	1·06	0·80	0·63	0·60	0·60	0·50	1·14	1·13	1·48	1·39	0·50	0·55	1·36	1·53	1·49	1·39	0·96	1·02	0·92	0·27	0·23
Dy	1·94	1·55	1·34	0·42	0·46	0·45	1·21	1·12	1·62	1·59	0·41	0·45	1·56	1·85	1·69	1·76	0·91	0·88	0·87	0·31	0·30
Ho	0·47	0·36	0·34	0·07	0·07	0·08	0·21	0·21	0·36	0·33	0·08	0·09	0·29	0·28	0·30	0·29	0·14	0·13	0·13	0·06	0·05
Er	1·42	1·12	1·00	0·21	0·24	0·23	0·46	0·48	0·92	0·89	0·22	0·21	0·74	0·72	0·73	0·71	0·32	0·28	0·30	0·13	0·14
Tm	0·18	0·17	0·14	0·04	0·03	0·04	0·06	0·06	0·11	0·12	0·03	0·03	0·07	0·09	0·08	0·08	0·03	0·03	0·03	0·02	0·02
Yb	1·36	1·26	1·23	0·23	0·20	0·20	0·28	0·31	0·62	0·60	0·15	0·15	0·32	0·30	0·31	0·31	0·14	0·12	0·12	0·10	0·09
Lu	0·22	0·20	0·15	0·04	0·03	0·04	0·03	0·04	0·09	0·08	0·02	0·02	0·04	0·03	0·03	0·04	0·01	0·01	0·01	<0·01	<0·01
Hf	0·12	0·10	0·08	0·20	0·17	0·18	0·41	0·39	0·22	0·27	0·24	0·21	0·46	0·54	0·56	0·47	0·10	0·11	0·10	0·02	0·06
Ta	0·01	0·01	0·01	0·04	0·05	0·05	0·06	0·05	0·01	0·01	0·09	0·08	0·02	0·03	0·02	0·02	0·02	0·02	0·02	<0·01	<0·01
Th	0·23	0·22	0·18	0·16	0·19	0·19	0·05	0·04	0·01	0·01	0·08	0·09	0·03	0·02	0·02	0·02	0·07	0·06	0·07	0·01	<0·01
U	0·04	0·05	0·05	0·02	0·03	0·02	0·02	0·02	<0·01	<0·01	0·03	0·03	0·01	0·01	0·01	0·01	0·02	0·02	0·02	<0·01	<0·01

(continued)

Table 8: Continued

	Spinel–garnet-peridotites									Garnet-peridotites								
Sample:	Pra299	Pra299	Pra299c	Pra299r	Pra399	Pra399	Pra399	Pra399	Pra399	Pra199r	Pra199c	Pra199r	Pra199r	Pra199c	Pra199	Pra302c	Pra302r	Pra302c
Sc	22·4	21·9	21·3	23·9	28·9	28·5	30·1	28·4	29·6	29·4	27·8	27·3	29·2	30·7	31·3	21·9	23·4	23·8
V	220	220	223	216	214	224	226	233	237	265	266	270	251	265	257	231	224	225
Co	26·9	28·2	28·4	28·1	28·9	30·2	28·9	28·8	28·9	33·6	31·5	31·8	30·5	32·0	30·6	28·4	28·7	28·0
Rb	0·04	0·03	0·04	0·02	0·01	0·03	0·02	0·02	0·01	0·01	0·01	0·01	0·01	0·01	0·01	0·01	0·01	0·02
Sr	0·26	0·24	0·58	0·34	118	117	118	118	114	84·8	82·9	80·9	81·8	83·1	81·3	1·78	1·65	1·79
Y	1·16	1·15	1·21	1·17	5·66	5·14	5·86	5·16	5·47	5·58	4·97	5·04	5·26	5·41	5·72	1·69	1·94	1·86
Zr	0·06	0·07	0·16	0·07	19·0	18·1	19·1	18·3	19·9	20·7	20·0	18·8	21·4	22·2	21·8	0·45	0·30	0·43
Nb	0·11	0·08	0·14	0·09	0·92	0·88	0·70	0·78	0·70	0·26	0·23	0·21	0·25	0·24	0·25	0·08	0·07	0·08
Ba	0·70	1·06	1·02	1·81	0·25	0·16	0·1	0·16	0·13	0·07	0·09	0·07	0·08	0·07	0·06	1·50	1·32	1·50
La	0·01	0·04	0·03	0·07	2·11	2·07	1·94	2·11	1·99	1·11	1·06	1·01	1·15	1·08	1·08	0·03	0·05	0·04
Ce	0·01	0·05	0·03	0·13	7·61	8·01	7·75	7·87	7·47	3·97	4·10	3·95	3·91	4·09	3·88	0·09	0·11	0·09
Pr	<0·01	<0·01	<0·01	0·02	1·19	1·14	1·13	1·2	1·13	0·77	0·76	0·74	0·71	0·79	0·71	0·03	0·03	0·03
Nd	0·03	0·06	0·04	0·16	5·37	5·25	4·96	4·89	5·16	4·20	4·45	4·07	4·32	4·42	4·60	0·42	0·34	0·44
Sm	0·12	0·13	0·11	0·12	1·4	1·66	1·53	1·58	1·66	1·47	1·32	1·44	1·57	1·65	1·50	0·25	0·22	0·34
Eu	0·06	0·06	0·05	0·07	0·46	0·56	0·54	0·53	0·52	0·50	0·54	0·50	0·54	0·54	0·55	0·13	0·12	0·13
Tb	0·05	0·06	0·05	0·06	0·22	0·24	0·23	0·21	0·25	0·23	0·23	0·23	0·26	0·26	0·23	0·07	0·07	0·09
Gd	0·22	0·22	0·24	0·34	1·58	1·52	1·56	1·36	1·57	1·64	1·47	1·52	1·77	1·60	1·67	0·43	0·41	0·38
Dy	0·30	0·30	0·31	0·36	1·39	1·36	1·46	1·26	1·24	1·22	1·15	1·24	1·32	1·28	1·30	0·41	0·45	0·42
Ho	0·05	0·05	0·05	0·06	0·23	0·22	0·25	0·20	0·23	0·22	0·18	0·18	0·19	0·22	0·21	0·07	0·08	0·08
Er	0·12	0·13	0·11	0·13	0·40	0·49	0·5	0·45	0·45	0·44	0·41	0·44	0·47	0·43	0·43	0·14	0·16	0·14
Tm	0·02	0·02	0·02	0·02	0·06	0·07	0·06	0·06	0·06	0·05	0·04	0·05	0·04	0·05	0·05	0·02	0·02	0·02
Yb	0·09	0·10	0·12	0·14	0·32	0·31	0·37	0·37	0·37	0·25	0·26	0·26	0·25	0·30	0·31	0·08	0·10	0·10
Lu	<0·01	0·01	<0·01	0·00	0·04	0·03	0·04	0·03	0·04	0·03	0·03	0·03	0·04	0·04	0·03	0·01	0·01	0·01
Hf	0·01	0·05	0·01	0·04	0·66	0·65	0·71	0·66	0·70	0·73	0·76	0·73	0·73	0·75	0·77	0·06	0·06	0·08
Ta	<0·01	<0·01	<0·01	<0·01	0·09	0·11	0·1	0·10	0·07	0·02	0·02	0·02	0·03	0·03	0·02	<0·01	<0·01	<0·01
Th	0·01	0·01	0·01	0·01	0·08	0·05	0·08	0·08	0·06	0·01	0·01	0·01	0·01	0·01	0·01	0·01	0·01	0·01
U	<0·01	<0·01	<0·01	<0·01	0·02	0·02	0·03	0·03	0·02	<0·01	<0·01	<0·01	<0·01	<0·01	<0·01	<0·01	<0·01	<0·01

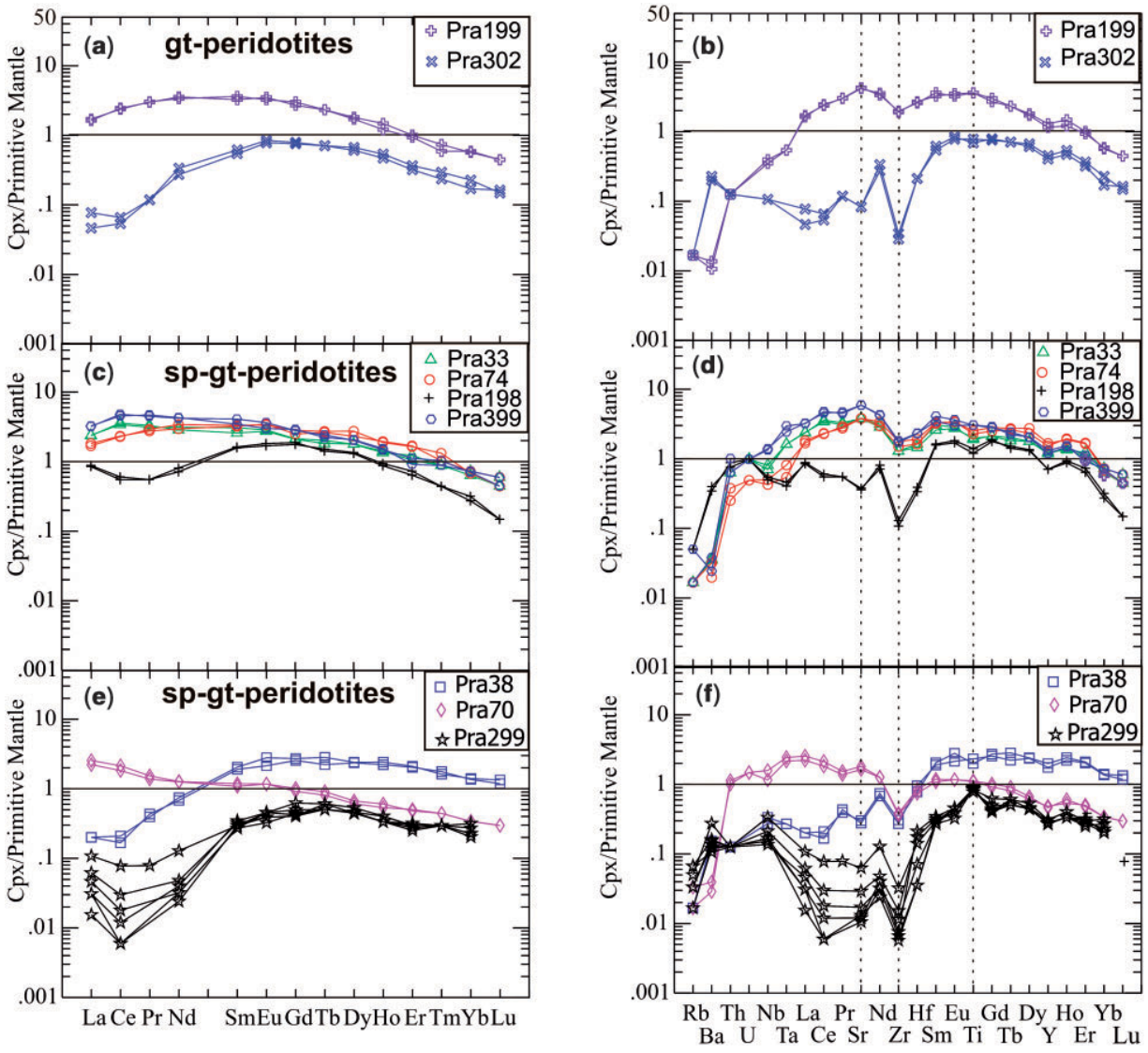

Fig. 8. Primitive Mantle normalized clinopyroxene REE and multi-element patterns of garnet-peridotites and spinel–garnet-peridotites [Primitive Mantle normalization values after McDonough & Sun (1995)].

subcontinental lithosphere 'ages' of 30 and 10 Ma, respectively (Fig. 11).

DISCUSSION

P–T conditions

For garnet-bearing samples, equilibrium T estimates (Table 11) were calculated based on the compositions of coexisting garnet, clinopyroxene and orthopyroxene. For spinel-bearing samples the compositions of coexisting clinopyroxene and orthopyroxene were used (Brey & Köhler, 1990). Pressure estimates were made using Al concentrations in orthopyroxene coexisting with garnet (Brey & Köhler, 1990). As discussed above, the major element compositions of olivine, orthopyroxene, clinopyroxene and garnet are homogeneous and, therefore, the calculated P–T conditions directly represent the environment at the time the xenoliths were entrained. T_{equil} values are high, ranging from 1060 to 1216°C. Calculated P_{equil} values for garnet-bearing peridotites are relative low, ranging from 18 to 23 kbar (Fig. 12). Extrapolating this geotherm into the spinel-peridotite field and taking into account the estimated temperatures for the Prahuaniyeu spinel-lherzolite xenoliths gives an inferred P_{equil} ranging from 15 to 20 kbar for the spinel-peridotites. Comparison of the inferred P_{equil} from the geotherm with the estimated P_{equil} based on the Ca exchange between coexisting olivine and

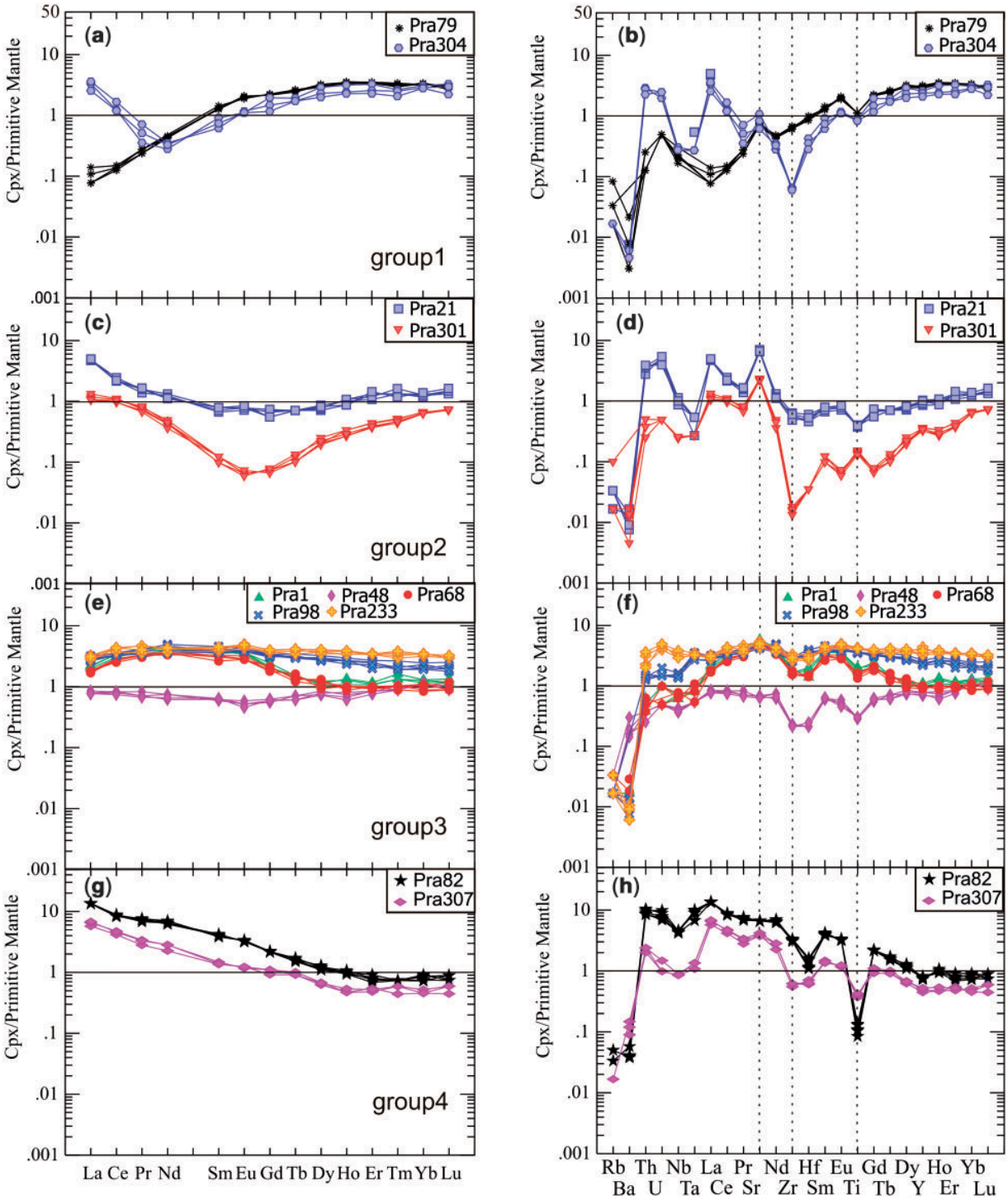

Fig. 9. Primitive Mantle normalized clinopyroxene REE and multi-element patterns for spinel-peridotites [Primitive Mantle normalization values after McDonough & Sun (1995)].

Table 9: LA-ICP-MS analyses, in ppm, of garnets from Prahuaniyeu peridotite xenoliths, northern Patagonia, Argentina

	Spinel–garnet-peridotites													
Sample:	Pra33	Pra33	Pra33	Pra33	Pra38	Pra38	Pra38	Pra70	Pra74	Pra74	Pra74	Pra198	Pra198	Pra198
Sc	153	156	160	145	180	181	180	159	170	164	183	125	120	125
V	118	118	118	120	82·0	74·5	78·1	157	99·8	97·2	96·6	104	102	98·0
Co	43·4	44·2	44·5	44·4	39·4	38·9	39·4	40·5	41·8	44·9	43·9	40·2	39·6	38·7
Ni	98·8	131	102	105	53·1	52·1	49·9	87·5	82·1	81·3	88·6	73·60	71·6	60·2
Rb	0·02	0·02	0·04	0·03	0·05	0·04	0·05	0·03	0·01	0·03	0·02	0·06	0·02	0·02
Sr	0·32	0·32	0·31	0·28	0·10	0·12	0·10	0·22	0·35	0·30	0·29	0·50	0·06	0·08
Y	44·7	46·4	46·0	37·8	77·9	72·4	74·9	22·1	42·5	44·1	42·0	32·8	28·6	33
Zr	37·5	34·5	34·4	31·1	7·81	7·87	7·19	18·4	35·3	35·9	33·3	3·85	3·17	3·63
Nb	0·25	0·22	0·25	0·20	0·08	0·10	0·08	0·97	0·13	0·15	0·18	0·13	0·23	0·23
Ba	0·01	0·00	−0·07	0·01	0·02	0·05	0·05	0·02	−0·01	0·05	0·03	0·00	0·04	0·03
La	0·02	0·02	0·02	0·01	0·00	0·00	0·01	0·03	0·01	0·01	0·01	0·02	0·01	0·01
Ce	0·19	0·22	0·22	0·18	0·01	0·01	0·01	0·19	0·13	0·12	0·13	0·15	0·05	0·04
Pr	0·05	0·06	0·07	0·05	0·01	0·01	0·01	0·04	0·06	0·05	0·05	0·06	0·01	0·02
Nd	0·49	0·55	0·51	0·51	0·14	0·18	0·12	0·40	0·53	0·56	0·56	0·86	0·17	0·24
Sm	0·59	0·74	0·70	0·53	0·53	0·51	0·68	0·63	0·71	0·71	0·70	1·01	0·40	0·48
Eu	0·44	0·47	0·46	0·43	0·39	0·38	0·31	0·32	0·49	0·49	0·44	0·70	0·26	0·33
Tb	0·60	0·63	0·60	0·50	0·85	0·79	0·74	0·40	0·59	0·55	0·57	0·85	0·46	0·51
Gd	2·20	2·26	2·13	1·83	2·84	2·72	2·39	1·61	2·52	2·48	2·56	3·46	1·76	2·41
Dy	6·01	6·26	6·22	5·13	9·23	9·09	8·15	3·38	5·39	5·67	5·39	8·00	4·10	5·20
Ho	1·62	1·70	1·68	1·37	2·92	2·72	2·42	0·84	1·56	1·61	1·52	2·21	1·20	1·36
Er	5·59	5·99	5·87	4·83	11·03	10·86	9·36	2·91	5·34	5·51	5·43	7·40	4·04	4·46
Tm	1·01	1·03	1·02	0·81	2·13	2·10	1·81	0·49	0·94	0·92	0·93	1·17	0·67	0·81
Yb	7·87	8·73	8·27	6·72	19·93	18·52	15·80	4·01	8·13	7·25	7·08	9·57	5·61	6·19
Lu	1·13	1·23	1·27	0·96	3·30	3·27	2·30	0·63	1·15	1·19	0·99	1·36	0·79	0·90
Hf	0·61	0·52	0·47	0·41	0·33	0·29	0·29	0·53	0·60	0·54	0·52	1·00	0·18	0·29
Ta	<0·01	<0·01	<0·01	<0·01	<0·01	<0·01	<0·01	0·03	0·01	0·01	0·01	0·01	<0·01	<0·01
Th	0·01	0·01	<0·01	<0·01	<0·01	<0·01	<0·01	0·01	<0·01	<0·01	<0·01	<0·01	<0·01	<0·01
U	0·01	0·01	0·01	<0·01	<0·01	<0·01	<0·01	0·02	<0·01	0·01	0·01	<0·01	0·01	0·01

	Spinel–garnet-peridotites					Garnet-peridotites								
						profile								
						core				rim				
Sample:	Pra299	Pra299	Pra299	Pra399	Pra399	Pra199	Pra199	Pra199	Pra199	Pra199	Pra302	Pra302	Pra302	Pra302
Sc	134	132	133	128	133	103	102	103	104	103	144	138	151	149
V	148	145	149	79·1	80·2	124	116	124	120	120	135	137	131	136
Co	41·6	39·4	41·6	43·1	39·3	58·2	54·7	57·9	55·7	55·8	46·3	47·5	45	46·4
Ni	83·1	87·5	88·3	64·3	67·1	108	102	108	103	106	82·9	88·4	82·5	82·7
Rb	0·02	0·01	0·02	0·02	0·04	0·06	0·04	0·04	0·02	0·03	0·02	0·02	0·01	0·03
Sr	0·04	0·07	0·05	0·46	0·46	0·50	0·35	0·37	0·36	0·30	0·03	0·04	0·03	0·04
Y	17·5	17·3	18·1	52·2	56·2	54·2	47·2	45·2	36	34·3	25·7	24·9	24·4	25·2
Zr	0·25	0·21	0·17	31·9	35·1	65·5	53·3	49·8	40·0	37·0	1·82	1·85	1·68	1·66
Nb	0·11	0·16	0·08	0·10	0·18	0·13	0·14	0·11	0·10	0·12	0·09	0·07	0·08	0·08
Ba	0·02	0·01	0·04	0·04	0·07	<0·01	0·01	0·01	0·01	0·01	<0·01	<0·01	<0·01	<0·01
La	0·01	0·01	0·01	0·01	0·02	0·02	0·01	0·01	0·01	0·01	<0·01	<0·01	<0·01	<0·01
Ce	0·00	0·01	0·01	0·17	0·18	0·15	0·15	0·14	0·12	0·12	<0·01	<0·01	<0·01	0·01
Pr	<0·01	<0·01	<0·01	0·05	0·07	0·06	0·07	0·05	0·05	0·05	0·01	0·01	0·01	0·01
Nd	0·04	0·05	0·05	0·49	0·77	0·86	0·71	0·68	0·64	0·57	0·07	0·07	0·09	0·10
Sm	0·09	0·13	0·17	0·90	0·95	1·01	0·90	0·84	0·77	0·61	0·24	0·29	0·26	0·23
Eu	0·07	0·10	0·14	0·62	0·63	0·70	0·59	0·63	0·47	0·51	0·21	0·20	0·18	0·22
Tb	0·25	0·28	0·29	0·74	0·75	0·85	0·68	0·71	0·53	0·56	0·33	0·32	0·32	0·37
Gd	1·04	0·82	0·84	3·68	3·18	3·46	2·88	2·82	2·35	2·28	1·10	1·19	1·26	1·13
Dy	2·22	2·09	2·15	7·14	7·67	8·00	6·84	6·34	5·06	4·60	3·72	3·44	3·22	3·57
Ho	0·70	0·69	0·70	1·89	2·14	2·21	1·73	1·53	1·22	1·21	1·01	0·92	0·94	0·96
Er	2·20	2·05	2·20	7·07	7·31	7·40	5·70	5·35	4·05	3·69	3·60	3·44	3·09	3·29
Tm	0·38	0·42	0·37	1·17	1·33	1·17	0·96	0·84	0·64	0·57	0·57	0·51	0·49	0·50
Yb	3·62	3·54	3·91	8·58	10·35	9·57	7·04	6·47	4·71	4·54	4·60	4·22	4·21	4·00
Lu	0·50	0·52	0·47	1·37	1·64	1·36	1·04	1·00	0·70	0·62	0·67	0·69	0·57	0·62
Hf	0·08	0·07	0·08	0·62	0·59	1·00	0·83	0·66	0·64	0·56	0·16	0·13	0·13	0·12
Ta	<0·01	<0·01	<0·01	0·01	<0·01	0·01	<0·01	<0·01	<0·01	0·01	0·01	<0·01	<0·01	<0·01

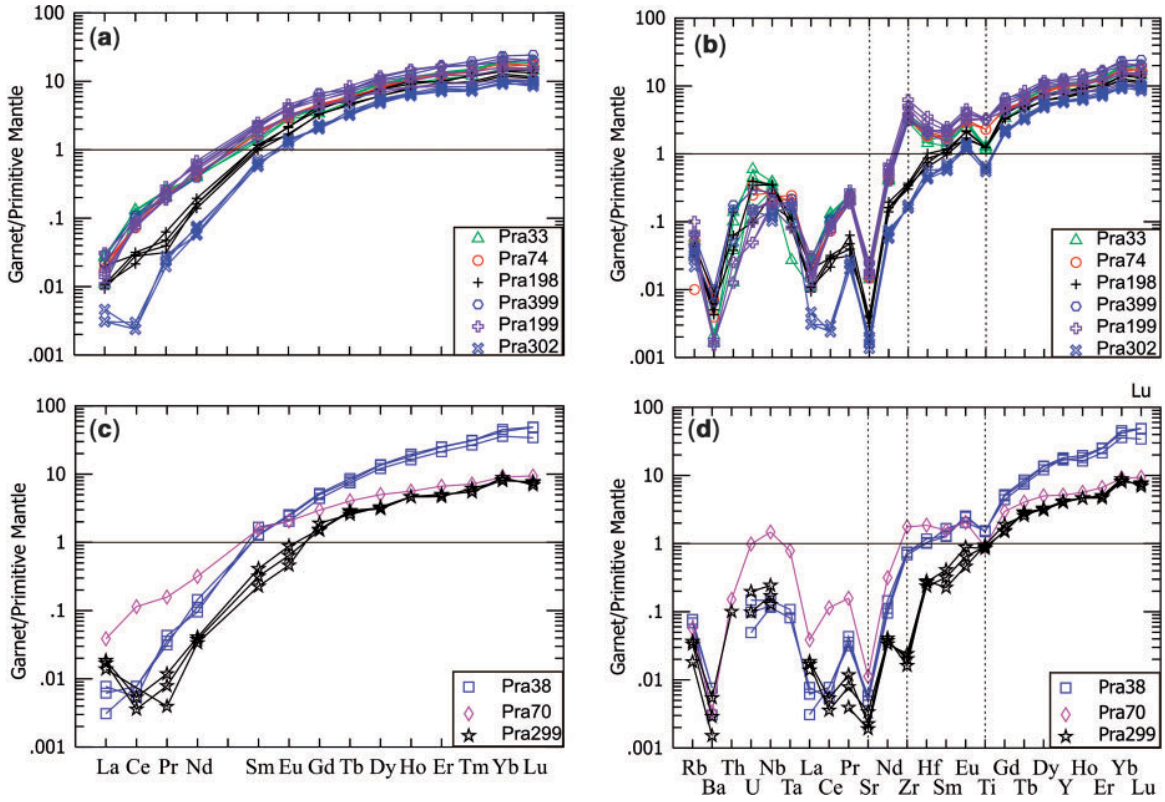

Fig. 10. Primitive Mantle normalized garnet REE and multi-element abundance patterns for garnet-peridotites [Primitive Mantle normalization values after McDonough & Sun (1995)].

Table 10: Whole-rock and mineral separate Nd isotope analyses

Sample	Sm (ppm)	Nd (ppm)	$^{147}Sm/^{144}Nd$	$^{143}Nd/^{144}Nd$	$\pm 2\sigma$
Pra199					
wr	1·038	0·380	0·221340	0·513139	0·000011
gt	0·554	0·861	0·940620	0·513287	0·000024
cpx	4·646	2·077	0·270340	0·513158	0·000010
opx	0·033	0·060	0·329037	0·513156	0·000013
Pra74					
gt	0·613	0·449	0·825850	0·513187	0·000026
cpx	1·427	4·021	0·214640	0·513144	0·000004
opx	0·029	0·052	0·332820	0·513145	0·000047
Pra1					
cpx	1·453	5·192	0·169260	0·512637	0·000005

Table 11: P–T estimates for Prahuaniyeu garnet- and spinel-peridotites

Sample	*T*	*P*	*P* Ca-in-Olivine
Gt-peridotites			
Pra33	1215	22·3	
Pra38	1144	17·8	
Pra70	1221	23·8	
Pra74	1192	22·4	
Pra198	1109	18·2	
Pra199	1216	22·6	
Pra234	1117	19·5	
Pra297	1156	19·8	
Pra299	1184	22·1	
Pra399	1144	17·8	
Pra420	1210	21·8	
Pra421	1134	19·2	
Sp-peridotites			
Pra1	1061	*15·0*	14·0
Pra68	1100	*17·0*	13·5
Pra91	1142	*20·0*	19·6
Pra94	1160	*20·0*	18·9
Pra96	1122	*17·0*	17·0
Pra98	1062	*15·0*	11·8

Pressures in italics are inferred from the geotherm in Fig. 12. *P* Ca-in-olivine, estimated pressures using the Köhler & Brey (1990) geobarometer.

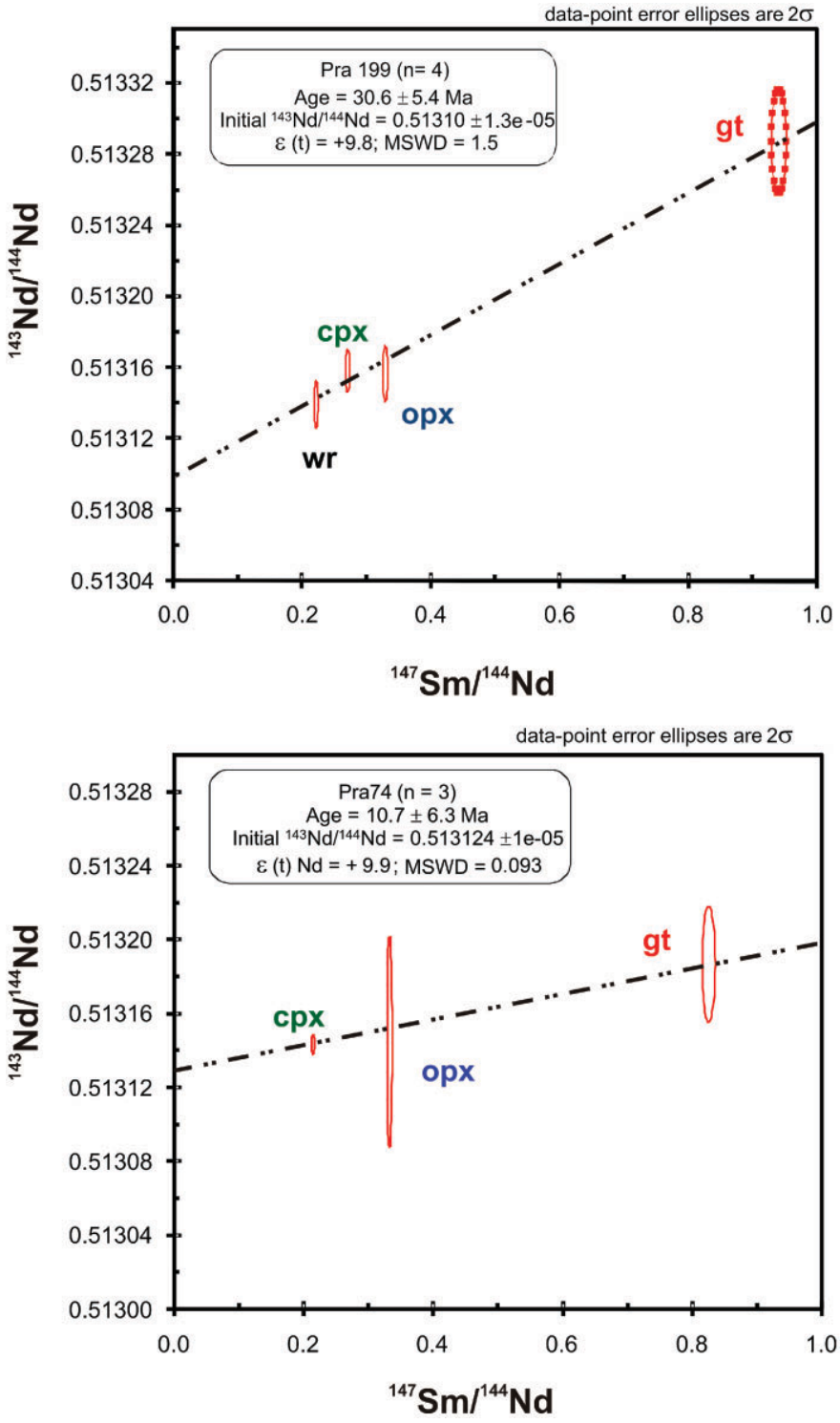

Fig. 11. Nd–Sm isochron diagrams showing the apparent age of garnet-peridotite Pral99 and spinel–garnet-peridotite Pra74.

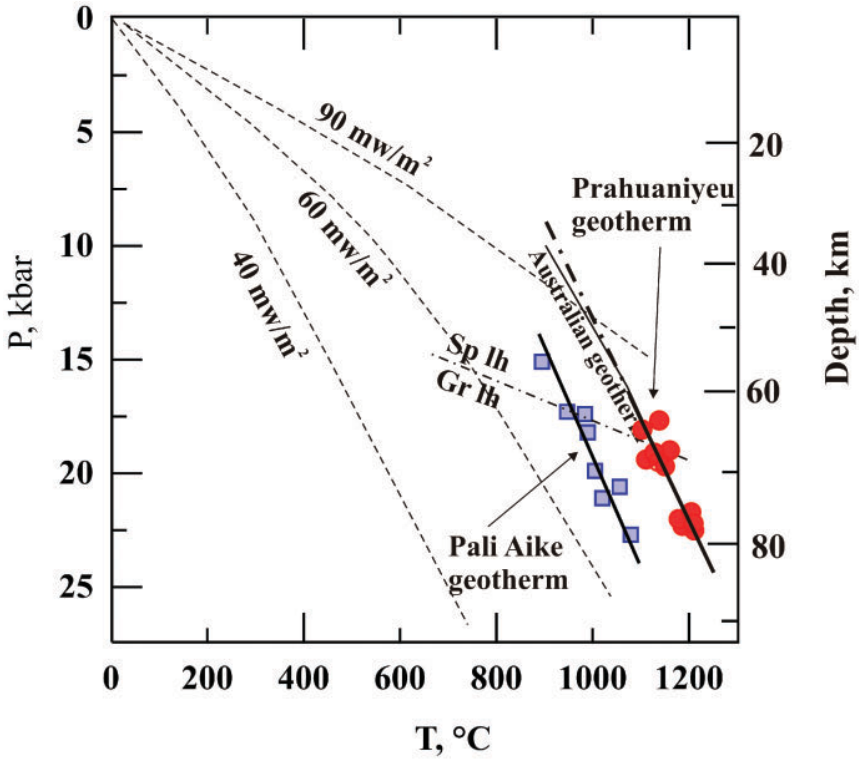

Fig. 12. *P–T* calculations for the Prahuaniyeu xenolith suite.

clinopyroxene (Köhler & Brey, 1990) shows a broad agreement between these two methods (Table 11), considering the strong temperature dependence and the analytical uncertainties of the Ca-in-olivine barometer (O'Reilly *et al.*, 1997).

In the *P–T* diagram, the Prahuaniyeu garnet-bearing xenoliths define a steep geotherm that plots between the model curves for heat flows of 80–100 mW/m^2 of Pollack & Chapman (1977). This is very similar to the geotherm constructed by O'Reilly & Griffin (1985) for the xenoliths from southeastern Australia (Fig. 12). These high temperatures at relatively low pressures require a high local heat flow; in southeastern Australia this has been attributed to an upwelling and underplating of basaltic magma associated with the opening of the Tasman Sea (O'Reilly & Griffin, 1985). Unfortunately, geophysical data, such as seismic refraction and reflection profiles, do not exist for the study area. In Prahuaniyeu the steep geotherm appears to be related to the evolution of the Late Oligocene Somoncura Large Igneous Province. Local mantle thermal instabilities caused by plate reorganization at that time could have been responsible for a plume-like mantle instability that caused the magmatism in this area (Kay *et al.*, 2007). Kay *et al.* (2007) reported isotopic compositions for the Somoncura province lavas comparable with those of plume-related basalts. Muñoz *et al.* (2000) proposed a slab window origin for the Somoncura Large Igneous Province in a generally extensional tectonic setting rather than a plume-like event. The resultant thermal anomaly could have been responsible for convective heat transport into the overlying lithosphere during the magmatic activity. The age of the xenolith-bearing basalts is not well known, although the age difference between the xenolith-bearing basalts and the Somoncura plateau lavas cannot be large, as the cooling of the lithosphere after a thermal perturbation is relatively fast and therefore the high equilibrium temperatures cannot be maintained for long. Sass & Lachenbruch (1979) have shown that cooling time constants are around 10 Ma, which implies that the age difference could not be more than 10 Myr.

The two most fertile samples, which gave apparent internal 'ages' between *c.* 10 and 30 Ma (including clinopyroxene, orthopyroxene, garnet and the whole-rock; Fig. 11) for the sub-Prahuaniyeu lithospheric mantle, suggest resetting of the Sm–Nd isotopic system under a high-temperature regime and most probably reflect closure of the system following this 'high-*T* event'. This, together with the evidence given by Kay *et al.* (2007), supports the existence of a plume or plume-like component in this area.

Whole-rock chemistry

Linear trends in correlation diagrams between major elements for mantle xenolith suites have been attributed

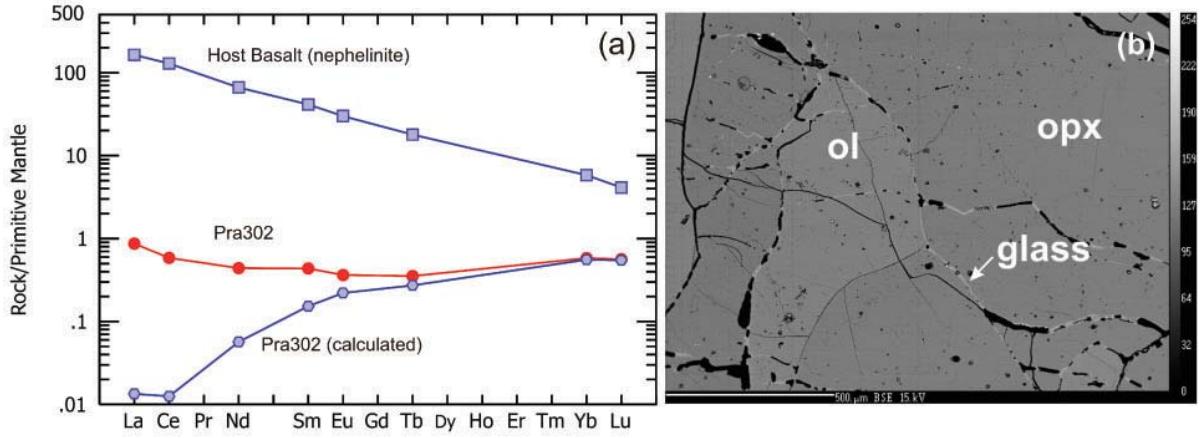

Fig. 13. Primitive mantle-normalized REE patterns showing that (a) garnet-peridotite Pra302 has experienced 0·5% host basalt (Pra2 nephelinite) infiltration. Pra302(calculated) is based on a mass-balance calculation using the garnet and clinopyroxene REE compositions and their modal percentage in Pra302 (Table 1). (b) BSE image of Pra302 shows thin films of intergranular melt (glass), the result of host basalt infiltration.

to variable degrees of partial melting of the same initial fertile mantle source (Frey & Green, 1974; Ionov *et al.*, 1993). This is not valid for the garnet-peridotite sample Pra302, whose composition might reflect mechanical mineral sorting. Whole-rock Al_2O_3 and CaO contents indicate a fertile mantle protolith (CaO is even higher than the Primitive Mantle) but TiO_2 and REE concentrations are consistent with a relatively depleted mantle source. As hydrous phases, with the exception of a single phlogopite grain, are not present in the studied xenoliths, host basalt infiltration and/or cryptic metasomatism is required to account for the observed whole-rock LREE enrichment (Fig. 5). Anhydrous modal metasomatism, involving addition of garnet and clinopyroxene to a depleted source, could be another possibility. There are several lines of evidence that document the addition of clinopyroxene and garnet during metasomatism. Chemical zoning, disequilibria and LREE enrichment are the main characteristics of metasomatic garnet and clinopyroxene (Shimizu, 1999; Simon *et al.*, 2003). The garnet-peridotite Pra302 does not show any of these features: (1) there is no chemical zoning; (2) the incompatible trace element abundances of garnet and clinopyroxene indicate equilibrium between them; (3) compared with the most fertile sample (Pra199), it is depleted in these elements (Figs 8 and 9). Petrographic evidence, however, is consistent with melt infiltration. BSE images show that this sample has been invaded by a melt that propagated between grains and filled up cracks in the rock-forming minerals (Fig. 13b). Indeed, the LREE enrichment is typical of host-melt infiltration, as the whole-rock REE pattern calculated from garnet and clinopyroxene REE concentrations (olivine and orthopyroxene were not considered for these calculations) has a convex-upward REE pattern. The LREE enrichment could have been caused by *c.* 0·5% basalt infiltration with a composition similar to that of the host basalt (Table 1, Fig. 13). The relative amount of host basalt added to Pra302 was calculated using the mass-balance relationship or 'lever rule' between Host Basalt (Table 2), Pra302(calculated) and Pra302 (Cox *et al.*, 1984). All these observations indicate that the protolith was depleted in incompatible elements, possibly as a result of mechanical mineral sorting.

Garnet-bearing xenoliths in alkali basalts are very rare; Prahuaniyeu is only the second known outcrop with such xenoliths in Patagonia, Pali Aike being the first. Thus comparison of the Prahuaniyeu garnet-bearing xenoliths with those from the Pali Aike Volcanic Field, the Vitim Volcanic Field (Baikal region) and from southeastern China (Xu *et al.*, 2000) is of particular interest. Recovered xenoliths indicate that the lithospheric mantle beneath Prahuaniyeu and Pali Aike experienced similar degrees of partial melting (Stern *et al.*, 1999). Pali Aike xenoliths span the range from fertile to depleted compositions, but the majority of the deep high-*P* garnet lherzolites are fertile. In the Vitim Volcanic Field, garnet and spinel–garnet lherzolites are fertile (Ionov *et al.*, 1993; Litasov & Taniguchi, 2002). For a given Al_2O_3 content, the fertile garnet-lherzolites from Pali Aike have systematically lower CaO contents than the Prahuaniyeu xenoliths, and, according to Stern *et al.* (1989), represent mixtures of infertile residual Mg-rich harzburgites and basaltic magma. On the other hand, with the exception of some depleted peridotites, the majority of the mantle-derived xenoliths from southeastern China are fertile peridotites (Xu *et al.*, 2000). The Pali Aike and southeastern China peridotites have experienced modal hydrous metasomatism (amphibole and/or phlogopite are present) whereas the Prahuaniyeu peridotites, like the Vitim peridotites, show

evidence for mainly cryptic metasomatism (Glaser *et al.*, 1999).

Trace elements in clinopyroxene and garnet

Trace element abundances in clinopyroxene and garnet indicate that the subcontinental lithospheric mantle beneath Prahuaniyeu is extremely inhomogeneous, having been affected by various melting and metasomatic processes. The major difference between clinopyroxenes from garnet-bearing and spinel-bearing xenoliths is the absence of negative Ti-anomalies in the former compared with Eu and Gd in mantle-normalized diagrams (Figs 8 and 9); for example, clinopyroxenes from southeastern China garnet-bearing xenoliths show only a weak Ti-anomaly (Xu *et al.*, 2000). Clinopyroxenes from Cape Verde spinel-bearing xenoliths do not have a Ti-anomaly because they experienced variable degrees of partial melting in the garnet-peridotite field (Bonadiman *et al.*, 2005). Thus the behavior of Ti clearly depends on the presence of garnet as the aluminous phase. The most pronounced negative Ti-anomaly was observed in the clinopyroxenes from spinel-peridotite Pra82. This sample has the highest $(La/Yb)_{PM}$, ranging from 15·0 to 19·5, and the lowest Ti/Eu ratio (200–300). Except for Nb and Zr, which show negative anomalies with respect to their neighbours, an overall elevation of incompatible elements can be observed (Figs 8 and 9). Coltorti *et al.* (1999) suggested that such extreme values are a signature of carbonatitic metasomatism; they are very similar to those in other mantle xenoliths that have been metasomatized by CO_2-rich fluids or carbonatitic melts. The fact that the relative depletion of Ti in the spinel-peridotite field cannot be modeled using common experimental mineral–melt partition coefficients (Norman, 1998) led Xu *et al.* (2000) to propose a much lower Ti_{Kd}, arguing that determinations of Ti_{Kd} based on the distribution of Ti between melt and Al-rich pyroxene are not applicable for magnesian Cr-diopsides from the Earth's mantle. Experimental data have also shown that increasing Al^{iv} increases the Ti_{kd} (Ntaflos *et al.*, 2007, fig. 12 and references therein).

Zirconium contents in clinopyroxenes from both garnet- and spinel-bearing xenoliths show variable negative anomalies compared with Nd and Sm in mantle-normalized diagrams. Norman (1998) showed that the negative Zr-anomaly in clinopyroxenes from spinel-bearing xenoliths can be predicted by the distribution coefficients and is a consequence of melting in the upper mantle. In garnet, Zr concentrations also appear to be a function of the degree of melt extraction. Garnet trace element patterns from the most fertile samples have a positive Zr-anomaly compared with their neighbouring elements, but this becomes progressively more negative as the overall depletion of trace elements increases (Fig. 10b and d). Similarly, garnets from the most fertile peridotites have Zr/Y ratios of *c.* 1·0 (Griffin *et al.*, 1998), whereas garnets from moderately depleted peridotites have ratios of *c.* 0·1 and from the most depleted peridotites of *c.* 0·01. However, garnet-peridotites Pra199 and Pra302, which have similar clinopyroxene/garnet ratios and clinopyroxene + garnet modal compositions corresponding to similar fertility, differ in their Zr/Y ratios by a factor of 10. This indicates that the Pra302 protolith was depleted in incompatible elements.

With the exception of garnets from samples Pra70 and Pra299, all garnets are depleted in LREE and enriched in MREE and HREE. The garnets from fertile garnet lherzolite Pra199, as mentioned above, are characterized by different contents of REE in their cores and rims.

The spinel–garnet assemblage

In contrast to the Pali Aike (Kempton *et al.*, 1999a) and Vitim (Ionov *et al.*, 1993; Ionov, 2004) spinel–garnet-bearing peridotites, in which spinel is enclosed by garnet, indicating that garnet grew at the expense of spinel, the Prahuaniyeu spinels were found only in contact with garnet rims and in the matrix (Fig. 2c and d). The conditions under which garnet and spinel can coexist strongly depend on the bulk Cr-content. Experimental and thermodynamic data have shown that increasing bulk Cr-content dramatically increases the stability field of spinel at higher pressures (Nickel, 1986; Brey *et al.*, 1999; Klemme, 2004). For the fertile peridotites, there is a range of cr-number between zero and 0·2 where the bivariant field of coexisting spinel and garnet is very narrow (Klemme, 2004). The bulk cr-number ratio of the Prahuaniyeu spinel–garnet-bearing xenoliths lies within this narrow range (Table 1) and the estimated P–T conditions (Table 11) are consistent with the experimental and thermodynamic modeling of Klemme (2004). The fact that spinel is never found as an inclusion in garnet indicates that both phases formed independently in the narrow bivariant field (Fig. 14).

Modeling of the trace elements

The spinel-peridotite REE patterns indicate that the lithospheric mantle has been variably affected by metasomatic fluids or melts. The absence of hydrous minerals, such as amphibole and/or phlogopite, suggests that this metasomatism was cryptic. In many cases, the host basalt has invaded the xenoliths and propagated along mineral grain boundaries, building thin intergranular films and causing the enrichment of the whole-rock LREE concentrations. In sample Pra82, the whole-rock REE patterns are parallel to the clinopyroxene patterns, which rules out intergranular percolation of any melts or fluids and instead suggests metasomatism followed by recrystallization. The very low Ti/Nb and the high Zr/Hf ratios suggest that the metasomatic agent was of a carbonatitic nature (Dupuy *et al.*, 1992).

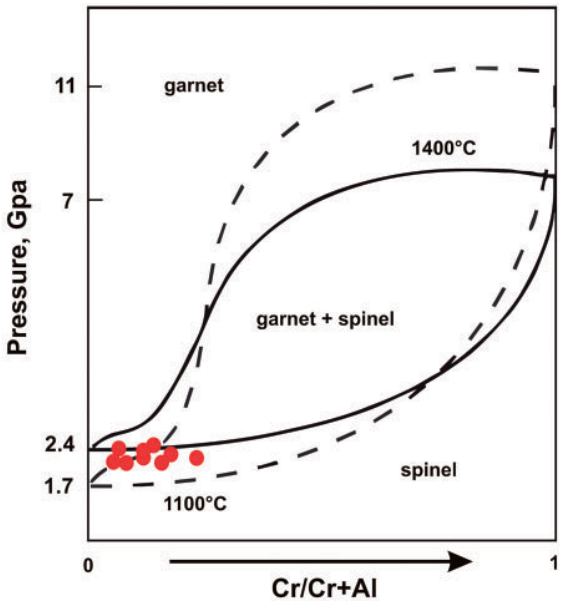

Fig. 14. Pressure vs whole-rock Cr/(Cr + Al) showing a narrow bivariate field of garnet + spinel (Klemme, 2004).

There are, however, some spinel-peridotites without any metasomatic signature and these, therefore, are appropriate for inferring the nature and degree of the melting processes. Using the distribution coefficients of Green *et al.* (2000), and the equations of Johnson *et al.* (1990), calculations show that sample Pra79 could be the residue after *c.* 5% fractional melting and the most depleted sample (Pra21) the residue of 12% fractional melting of a primitive mantle source. Sample Pra301, with Gd/Yb = 0·14, does not conform to these calculations and the REE pattern indicates multiple depletion and enrichment processes. Similar calculations for fertile garnet-bearing peridotites show that they have experienced 1–3% partial melting. In contrast, spinel–garnet-peridotite Pra299, which is the most depleted in incompatible elements, could be the residue after 13% partial melting of a primitive garnet-peridotite with 20 vol.% clinopyroxene and 15 vol.% garnet. However, such a parental garnet-peridotite modal composition is unrealistic (rough calculations show that the source garnet-peridotite should have had *c.* 6 wt% of Al_2O_3) and other processes must be invoked to account for the REE and other incompatible element patterns of this sample. Comparing the mineral compositions of this sample with those of sample Pra302, it is clear that Pra299 is more depleted in basaltic components than Pra302. Sample Pra302 is unique, as its whole-rock and modal compositions and major element mineral analyses classify it as a fertile garnet-lherzolite but its incompatible elements reflect the composition of a peridotite depleted in basaltic components. The extremely depleted garnet and clinopyroxene REE abundances of sample Pra299 can be modeled by 3% partial melting of a parental garnet-peridotite with the composition of sample Pra302.

The lithospheric mantle beneath Prahuaniyeu

The equilibrium *P–T* conditions indicate that the studied samples were entrained from depths between 40 and 80 km. This section of the upper mantle is inhomogeneous, varying from relatively fertile to very depleted in basaltic components. However, one of the most striking characteristics of the Prahuaniyeu mantle xenolith suite is the absence of hydrous minerals. In contrast to cryptic metasomatism, modal metasomatism has not occurred in this area. The Somoncura Large Igneous Province is the key to understanding the evolution of the lithospheric mantle in the study area. Kay *et al.* (2007) argued that the origin of the Somoncura Plateau basalts is associated with the melting of a plume-like mantle source mixed with melts of a phlogopite- and amphibole-rich lithospheric mantle, and that the hydrous phases are related to the dehydration of a disintegrated subducted slab. As mentioned above, in the section on *P–T* conditions, the calculated high temperatures at relatively low pressures require a local high heat flow, which also supports the ascending mantle plume model. However, with the exception of a single phlogopite grain, no hydrous phases have been found in the studied xenoliths, which were entrained by the host basalts from the same depth from which the Somoncura basalts were generated (Kay *et al.*, 2007). Moreover, trace element abundances in clinopyroxenes and garnets from the garnet-bearing xenoliths strongly suggest partial melting and not metasomatic processes. Furthermore, the cryptic metasomatism seen in a number of spinel-peridotite xenoliths does not provide evidence for involvement of slab-derived fluids from a subducted slab. In fact, data for some samples, for example Pr82 and Pr307, suggest that they experienced carbonatitic metasomatism. In addition, the undersaturated xenolith-bearing host basalts have characteristic negative K-anomalies. Such anomalies have been attributed to the presence of phlogopite or amphibole in the source material, which, after a low degree of partial melting, remains in the residue. If this is valid, other elements such as Ba, Nb and Ta, which are strongly partitioned into phlogopite or amphibole, should also be depleted in the host lavas, as is K. However, this is not the case, and the depletion must be related to a depleted source (Chauvel *et al.*, 1992).

The inferred apparent very young 'age' of the mantle lithosphere (~10–30 Ma) is not consistent with the age of the overlaying crust, which is Triassic and older (Pankhurst *et al.*, 2006). According to Schilling *et al.* (2008), Re–Os isotopic data for two spinel-peridotites from Prahuaniyeu provide an estimate of the time of the melting events, which ranges from 0·33 to 2·09 Ga.

The age resetting observed in the garnet-peridotites must be associated with a major heating event that, according to the literature (Kay *et al.*, 2007) and the calculated P–T conditions, could be an upwelling plume. The fact that no hotspot has been found associated with this plume led Kay *et al.* (2007) to suggest a model involving hydrous components derived from a subducted slab. In their model, these disintegrated at depth and, in combination with the heat provided by the plume-like upwelling, triggered the melting processes that led to the formation of the Somoncura Large Igneous Province. However, volatiles from the subducted oceanic crust could have affected the deep-seated upwelling plume as a result of its complete dehydration at shallow depths; only subducted peridotite can carry water into the deeper mantle (Schmidt & Poli, 1998). Consequently, large ion lithophile elements (LILE) will be depleted at the volcanic front, such that, at greater depths, a possible disintegrated slab involved in the melting processes will be enriched in high field strength elements (HFSE). This, in turn, implies that melts generated in such an environment would have an HFSE- rather than an LILE-enriched signature. The Prahuaniyeu garnet-peridotites were last equilibrated at depths between 70 and 90 km. These are, according to Kay *et al.* (2007), the generation depths of the voluminous main plateau magmas. Thus the model for magma generation with participation of slab-related components proposed by Kay *et al.* (2007) appears to be inconsistent with the geochemical and petrological data presented in this paper for the garnet-peridotites that have been exhumed to the surface by alkali basalts from the same depths. It would be expected that at least some of the garnet-peridotites would provide evidence for metasomatism (cryptic and/or modal).

CONCLUSIONS

Prahuaniyeu constitutes the second South American locality in which garnet-bearing peridotites have been found associated with intraplate alkali basalts. Spinel- and garnet-bearing peridotites cover the whole range between depleted and fertile mantle compositions, with the majority of the garnet-bearing peridotites being fertile.

The spinel-peridotites are the residues after 5–12% fractional melting, whereas the garnet-bearing peridotites are the residues after only 1–3% fractional melting. Clinopyroxenes from spinel-peridotites have negative Ti- and Zr-anomalies compared with their Primitive Mantle normalized neighbouring elements, whereas those from garnet-bearing peridotites do not show any anomaly, suggesting that their incompatibility during partial melting depends strongly on pressure.

The Zr content in garnets is a function of the degree of depletion in basaltic components. Thus garnet Primitive Mantle normalized incompatible trace element abundances that have a positive Zr-anomaly compared with Nd and Sm belong to the most fertile garnet-peridotites and those with a negative Zr-anomaly belong to the most depleted garnet-peridotites.

The spinel-bearing peridotites have experienced cryptic metasomatism. Carbonatitic metasomatism has been recognized in a number of samples. Garnet-bearing peridotites show only intergranular host basalt infiltration.

Estimated P–T equilibration conditions, with relatively high temperatures and low pressures, support the existence of local mantle thermal instabilities.

The 10–30 Ma calculated apparent internal 'ages' for the sub-lithospheric mantle in this region reflect a resetting of the Sm–Nd isotopic system in a high-temperature regime and most probably reflect closure of the system following this 'high-T event'. This lends further support to the postulated presence of mantle thermal instabilities.

ACKNOWLEDGEMENTS

We are grateful to Mike Tourbet, Memorial University of Newfoundland, for assistance with LA-ICP-MS, Monika Horschinegg for assistance with TIMS, and Cornelius Tschegg for technical support. This research was financially supported by the UNESCO IGCP Project Number 408 and Hochschuljubiläumsfonds der Stadt Wien and the ANPCYT of Argentina. We wish to thank M. Coltorti, W. L. Griffin and C. R. Stern for their constructive reviews and suggestions, which greatly improved the original manuscript. We are also indebted to H. Rice for improving the English. The editorial handling by M. Wilson is greatly appreciated.

REFERENCES

Arai, S. (1994). Compositional variation of olivine–chromian spinel in Mg-rich magmas as a guide to their residual spinel peridotites. *Journal of Volcanology and Geothermal Research* **59**, 279–293.

Bjerg, E. A., Ntaflos, T., Kurat, G., Dobosi, G. & Labudia, C. H. (2005). The upper mantle beneath Patagonia, Argentina, documented by xenoliths from alkali basalts. *Journal of South American Earth Sciences* **18**, 125–145.

Bonadiman, C., Beccaluva, L., Coltorti, M. & Siena, F. (2005). Kimberlite-like metasomatism and 'Garnet Signature' in spinel-peridotite xenoliths from Sal, Cape Verde Archipelago: relics of a subcontinental mantle domain within the Atlantic Oceanic Lithosphere? *Journal of Petrology* **46**, 2465–2493.

Brey, G. P. & Köhler, T. (1990). Geothermobarometry in four-phase lherzolites II. New thermobarometers, and practical assessment of existing thermobarometers. *Journal of Petrology* **31**, 1353–1378.

Brey, G. P., Doroshev, A.M., Girnis, A.V. & Turkin, A.I. (1999). Garnet–spinel–olivine–orthopyroxene equilibria in the FeO–MgO–Al_2O_3–SiO_2–Cr_2O_3 system: I. Composition and molar volumes of minerals. *European Journal of Mineralogy* **11**, 599–617.

Chauvel, C., Hofmann, A. W. & Vidal, P. (1992). HIMU-EM: The French Polynesian connection. *Earth and Planetary Science Letters* **110**, 99–119.

Coltorti, M., Bonadiman, C., Hinton, R. W., Siena, F. & Upton, B. G. J. (1999). Carbonatite metasomatism of the oceanic upper

mantle: evidence from clinopyroxenes and glasses in ultramafic xenoliths of Grande Comore, Indian Ocean. *Journal of Petrology* **40**, 133–165.

Cox, K. G., Bell, J. D. & Pankhurst, R. J. (1984). *The Interpretation of Igneous Rocks*. London: George Allen & Unwin.

Dawson, J. B., Powell, D. G. & Reid, A. M. (1970). Ultrabasic lava and xenoliths from the Lashaine volcano, northern Tanzania. *Journal of Petrology* **11**, 519–548.

Dupuy, C., Liotard, J. M. & Dostal, J. (1992). Zr/Hf fractionation in intraplate basaltic rocks: Carbonate metasomatism in the mantle source. *Geochimica et Cosmochimica Acta* **56**, 2417–2423.

Frey, F. A. & Green, D. H. (1974). The mineralogy, geochemistry and origin of lherzolite inclusions in Victorian basanites. *Geochimica et Cosmochimica Acta* **38**, 1023–1059.

Glaser, S. M., Foley, S. F. & Gunther, D. (1999). Trace element compositions of minerals in garnet and spinel peridotite xenoliths from the Vitim volcanic field, Transbaikalia, eastern Siberia. *Lithos* **48**, 263–285.

Gorring, M. L. & Kay, S. M. (2001). Mantle processes and source of Neogene slab window magmas from southern Patagonia, Argentinia. *Journal of Petrology* **42**, 1067–1094.

Gorring, M. L., Kay, S. M., Zeitler, P. K., Ramos, V. A., Rubiolo, D., Fernandez, M. I. & Panza, J. L. (1997). Neogene Patagonian plateau lavas: Continental magmas associated with ridge collision at the Chile triple junction. *Tectonics* **16**, 1–17.

Green, T. H., Blundy, J. D., Adam, J. & Yaxley, G. M. (2000). SIMS determination of trace element partition coefficients between garnet, clinopyroxene and hydrous basaltic liquids at 2–7·5 GPa and 1080–1200°C. *Lithos* **53**, 165–187.

Griffin, W. L., O'Reilly, S. Y., Ryan, C. G., Gaul, O. & Ionov, D. A. (1998). Secular variation in the composition of subcontinental lithospheric mantle: geophysical and geodynamic implications. In: Braun, J., Dooley, J. C., Goleby, B. R., Van Der Hilst, R. D. & Klootwijk C. T. (eds) *Structure and Evolution of the Australian Continent*. American Geophysical Union, Washington D.C., pp 1–26.

Henjes-Kunst, F. & Altherr, R. (1992). Metamorphic petrology of xenoliths from Kenya and northern Tanzania and implications for geotherms and lithospheric structures. *Journal of Petrology* **33**, 1125–1156.

Ionov, D. A., Ashchepkov, I. V., Stosch, H.-G., Witt-Eickschen, G. & Seck, H. A. (1993). Garnet peridotite xenoliths from the Vitim Volcanic Field, Baikal region: the nature of the garnet–spinel peridotite transition zone in the continental mantle. *Journal of Petrology* **34**, 1141–1175.

Ionov, D. A. (2004). Chemical variations in peridotite xenoliths from Vitim, Siberia: inferences for REE and Hf behaviour in the garnet facies upper mantle. *Journal of Petrology* **45**, 343–367.

Johnson, K. T. M., Dick, H. J. B. & Shimizu, N. (1990). Melting in the oceanic upper mantle: an ion microprobe study of diopsides in abyssal peridotites. *Journal of Geophysical Research* **95**, 2661–2678.

Kay, S. M., Ardolino, A. A., Gorring, M. L. & Ramos, V. A. (2007). The Somuncura Large Igneous Province in Patagonia: interaction of a transient mantle thermal anomaly with a subducting slab. *Journal of Petrology* **48**, 43–77.

Kempton, P. D., Haweskworth, C. J., Lopez-Escobar, L., Pearson, D. G. & Ware, A. G. (1999*a*). Spinel ± garnet lherzolite xenoliths from Pali Aike, Part 2: trace element and isotopic evidence on the evolution of lithospheric mantle beneath southern Patagonia. In: Gurney, J. J., Gurney, J. L., MD Pascoe, M. D. & Richardson, S. H. (eds) *T. J. B. Dawson Volume, Proceedings of the 7th International Kimberlite Conference*. Cape Town: Red Roof Design, pp. 415–428.

Kempton, P. D., Lopez-Escobar, L., Haweskworth, C. J., Pearson, D. G., Wright, D. W. & Ware, A. G. (1999*b*). Spinel ± garnet lherzolite xenoliths from Pali Aike, Part 1: Petrography, mineral chemistry and geothermobarometry. In: Gurney, J. J., Gurney, J. L., MD Pascoe, M. D. & Richardson, S. H. (eds) *T. J. B. Dawson Volume, Proceedings of the 7th International Kimberlite Conference*. Cape Town: Red Roof Design, pp. 403–414.

Klemme, S. (2004). The influence of Cr on the garnet–spinel transition in the Earth's mantle: experiments in the system MgO–Cr_2O_3–SiO_2 and thermodynamic modelling. *Lithos* **77**, 639–646.

Köhler, T. & Brey, G. P. (1990). Calcium exchange between olivine and clinopyroxene calibrated as a geothermobarometer for natural peridotites from 2 to 60 kb with applications. *Geochimica et Cosmochimica Acta* **54**, 2375–2388.

Kruse, H. & Spettel, B. (1979). A combined set of automatic and interactive programs for instrumental neutron activation analysis. *Journal of Radioanalytical Chemistry* **70**, 427–434.

Labudía, C. H. & Bjerg, E. A. (1994). Geologia del sector oriental de la hoja Bajo Hondo (39e), provincia de Río Negro. *Revista de la Asociación Geológica Argentina* **49**, 284–296.

Litasov, K. & Taniguchi, H. (2002). *Mantle Evolution beneath the Baikal Rift*. Center for Northeast Asian Studies, Tohoku University, Sendai, Japan.

Llambías, E. J. & Rapela, C. W. (1984). Geología de los Complejos Eruptivos de La Esperanza, provincia de Río Negro. *Revista de la Asociación Geológica Argentina* **39**, 220–243.

McDonough, W. F. & Sun, S.-s. (1995). The composition of the Earth. *Chemical Geology* **120**, 223–253.

Muñoz, J., Troncoso, R., Duhart, P., Cringola, P., Farmer, L. & Stern, C. R. (2000). The relation of the mid-Tertiary coastal magmatic belt in south–central Chile to the late Oligocene increase in plate convergence rate. *Revista Geológica de Chile* **27**, 177–203.

Nickel, K. G. (1986). Phase equilibria in the system SiO_2–MgO–Al_2O_3–CaO–Cr_2O_3 (SMACCR) and their bearing on spinel/garnet lherzolite relationships. *Neues Jahrbuch für Mineralogie, Abhandlungen* **155**, 259–287.

Norman, M. D. (1998). Melting and metasomatism in the continental lithosphere: laser ablation ICPMS analysis of minerals in spinel lherzolites from eastern Australia. *Contributions to Mineralogy and Petrology* **130**, 240–255.

Ntaflos, T., Bjerg, E. A., Labudia, C. H. & Kurat, G. (2007). Depleted lithosphere from the mantle wedge beneath Tres Lagos, southern Patagonia, Argentina. *Lithos* **94**, 46–65.

Nullo, F. E. (1978). Descripción geológica de la Hoja 41d, Lipetrén, provincia de Río Negro. *Servicio Geologico Nacional Boletin* **158**, 1–88.

O'Neil, H. S. C. & Palme, H. (1998). Composition of the Silicate Earth: Implication from accretion and core formation. In: Jackson, I. (ed.) *The Earth's Mantle Composition, Structure and Evolution*. Cambridge: Cambridge University Press, pp. 3–126.

O'Reilly, S. Y. & Griffin, W. L. (1985). A xenolith-derived geotherm for southeastern Australia and its geophysical implications. *Tectonophysics* **111**, 41–63.

O'Reilly, S. Y., Chen, D., Griffin, W. L. & Ryan, C. G. (1997). Minor elements in olivine from the spinel lherzolite xenoliths: implications for thermobarometry. *Minealogical Magazine* **61**, 257–269.

Pankhurst, R. J., Rapela, C. W., Fanning, C. M. & Márquez, M. (2006). Gondwanide continental collision and the origin of Patagonia. *Earth-Science Reviews* **76**, 235–237.

Pollack, H. N. & Chapman, D. S. (1977). On the regional variation of heat flow, geotherms and the thickness of the lithosphere. *Tectonophysics* **38**, 279–296.

Saini-Eidukat, B., Bjerg, E. A., Gregori, D. A., Beard, B. L. & Johnson, C. M. (1999). Jurassic granites in the northern portion of

the Somoncurá Massif, Río Negro, Argentina. In: Hanne, V. M. (ed.) Asociación Geológica Argentina, *XIV Congreso Geológico Argentino, Salta, Argentina*, Actas **II**, 175–177.

Sass, H. J. & Lachenbruch, H. A. (1979). Thermal regime of the Australian continental crust. In: McElhinny, M. W. (ed.) *The Earth, its Origin, Structure and Evolution*. London: Academic Press.

Schilling, M. E., Carlson, R. W., Conceição, R. V., Dantas, C., Bertotto, G. W. & Koester, E. (2008). Re–Os isotope constraints on subcontinental lithospheric mantle evolution of southern South America. *Earth and Planetary Science Letters* **268**, 89–101.

Schmidt, M. W. & Poli, S. (1998). Experimentally based water budgets for dehydrating slabs and consequences for arc magma generation. *Earth and Planetary Science Letters* **163**, 361–379.

Shimizu, N. (1999). Young geochemical features in cratonic peridotites from southern Africa and Siberia. In: Fei, Y., Bertka, C. M. & Mysen, B. O. (eds) *Mantle Petrology: Field Observations and High Pressure Experimentation. A Tribute to Francis R. (Joe) Boyd. Geochemical Society, Special Publication*, pp. 47–55.

Simon, N. S. C., Irvine, G. J., Davies, G. R., Pearson, D. G. & Carlson, R. W. (2003). The origin of garnet and clinopyroxene in 'depleted' Kaapvaal peridotites. *Lithos* **71**, 289–322.

Skewes, M. A. & Stern, C. R. (1979). Petrology and geochemistry of alkali basalts and ultramafic inclusions from the Palei-Aike volcanic field in southern Chile and the origin of the Patagonian plateau lavas. *Journal of Volcanology and Geothermal Research* **6**, 3–25.

Stern, C. R., Saul, S., Skewes, M. A. & Futa, K. (1989). Garnet peridotite xenoliths from the Pali-Aike alkali basalts of southernmost South America. In: Rossi, J. (ed.) *Kimberlites and Related Rocks. Geological Society of Australia Special Publication* **14**, 735–744.

Stern, C. R., Kilian, R., Olker, B., Hauri, E. H. & Kyser, T. K. (1999). Evidence from mantle xenoliths for relatively thin (<100 km) continental lithosphere below the Phanerozoic crust of southernmost South America. *Lithos* **48**, 217–235.

Stipanicic, P. N. & Methol, E. J. (1980). Comarca Norpatagónica. In: Leanza, E. F. (ed.) *Proceedings II Simposio de Geología Regional Argentina*. Córdoba: Academia Nacional de Ciencias, pp. 1071–1097.

Sutherland, F. L. & Hollis, J. D. (1982). Mantle–lower crust petrology from inclusions in basaltic rocks in Eastern Australia—an outline. *Journal of Volcanology and Geothermal Research* **14**, 1–29.

Wang, J., Hattori, K. H., Li, J. & Stern, C. R. (2008). Oxidation state of Paleozoic subcontinental lithospheric mantle below the Pali Aike volcanic field in southernmost Patagonia. *Lithos* **105**, 98–110.

Xu, X., O'Reilly, S. Y., Griffin, W. L. & Zhou, X. (2000). Genesis of young lithospheric mantle in southeastern China: an LAM-ICPMS trace element study. *Journal of Petrology* **41**, 111–148.

Zindler, A. & Hart, S. R. (1986). Chemical geodynamics. *Earth and Planetary Science Letters* **14**, 493–571.